

POLITECNICO DI TORINO

Collegio di Ingegneria Informatica, del Cinema e Meccatronica

Corso di Laurea Magistrale

in Ingegneria Meccatronica – Mechatronic Engineering

Master Thesis

Simulation of an active disc brake with hydro-mechanical torque control



Relatori

Prof. Luigi Mazza

Ing. Patrik Bordovsky

Candidata

Sara Hamed Adibpoor

Aprile 2018

Task

Hydraulic disc brakes are used in trains and light rail vehicles due to their high power density, compact design, and good dynamic performance. However, their generated braking torque is seldom a part of a closed-loop control and no counteracting action is usually taken against the several disturbances acting in the contact zone between brake pads and disc, where a variable friction coefficient arises. Consequently, phenomena such as brake fade and brake judder may occur, leading to passengers' uneasiness and degradation of the braking performance.

In the present work, an active brake disc of floating caliper type is analyzed, modelled and simulated and the effect of an inconsistent friction coefficient on its braking torque is highlighted. A closed loop concept is introduced and a hydro-mechanical control unit is embedded into the standardized brake design, to enhance the system behavior in presence of disturbances and to ensure accuracy and repeatability of the generated braking torque.

Table of contents

I	Formula symbols.....	iv
II	Abbreviations	vi
1	Introduction.....	7
2	Literature review	9
2.1	Brake systems on railway vehicles	9
2.1.1	General overview.....	9
2.1.2	Indirect pneumatic brakes.....	12
2.1.3	Direct pneumatic brakes	14
2.1.4	Direct electro pneumatic brakes	14
2.1.5	Magnetic brakes.....	15
2.1.6	Eddy currents brakes	15
2.1.7	Drum brakes	15
2.1.8	Disc brakes	16
2.2	Brake systems on tramway vehicles	17
2.2.1	Legal requirements	17
2.2.2	Design configuration	18
2.3	Potential losses of brake effectiveness.....	20
2.3.1	Brake fade.....	21
2.3.2	Brake judder	21
2.3.3	Solutions proposed in literature.....	22
3	Analysis of the actual brake system and mathematical model deployment.....	25
3.1	Analysis of the brake system HYA 48/72.....	25
3.2	Mathematical model of the open loop brake system.....	30
3.2.1	Proportional pressure reducing valve	31
3.2.2	Pipelines.....	33
3.2.3	Hydraulic actuator pressure dynamics.....	34
3.2.4	Brake assembly.....	36
3.2.5	Brake fluid	37
3.3	Mathematical model of the closed loop system	37
3.3.1	Closed loop concept description.....	37
3.3.2	Spool dynamics.....	39
3.3.3	Control pressure computation.....	39
3.3.4	System linearization	43
3.3.5	Closed loop system model summary	44
3.3.6	Closed loop system stability considerations	47
4	Simulation model and results analysis.....	50
4.1	Open loop simulation system	50
4.1.1	The hydraulic block: PPRV, pipeline connection and hydraulic actuator.....	51
4.1.2	The elastic contact block: pads-disc interface	56
4.1.3	The hydraulic fluid	58
4.1.4	Rotor-pad disc friction coefficient.....	59

4.1.5	Brake system kinematic model.....	60
4.1.6	Open loop simulation model results	63
4.2	Closed loop simulation model.....	66
4.2.1	Closed loop simulation model in Simulink	67
4.2.2	Closed loop simulation model in Amesim	68
4.2.3	Sensitivity analysis and parameters optimization.....	72
4.2.4	Closed loop simulation results and stability analysis	74
5	Summary and outlook	83
III	Literature.....	85
IV	List of figures.....	88
V	List of tables	91

I Formula symbols

μ	Pad-disc friction coefficient	[-]
A	Cubical expansion coefficient	[-]
A_p	Piston cross section	[m ²]
A_{pin}	Active surface of the control pin	[m ²]
B	Discharge coefficient	[1/(min·mm·√bar)]
C_h	Hydraulic capacitance	[l/bar]
c_{pad1}	Pad damping coefficient on inboard side	[Ns/m]
c_{pad2}	Pad damping coefficient on outboard side	[Ns/m]
D	Viscous friction coefficient	[Ns/m]
F_{b0}	Caliper stiction force	[N]
F_{fl}	Axial component of the flow force	[N]
F_{N1}	Clamping force on piston side	[N]
F_{N2}	Clamping force on fingers side	[N]
F_{p0}	Piston stiction force	[N]
F_{sol}	Solenoid force	[N]
F_{sp0}	Spring preload	[N]
I	Input current	[A]
k_{pad1}	Pad stiffness on inboard side	[N/m]
k_{pad2}	Pad stiffness on outboard side	[N/m]
k_{px}	Pressure sensitivity	[N/ m ³]
k_{qp}	Pressure/Flow gain	[m ⁵ /sN]
k_{qx}	Flow gain	[m ² /s]
k_{sol}	Solenoid constant	[N/A]
k_{spr}	Return spring stiffness	[N/m]
m_b	Caliper mass	[kg]
m_p	Piston mass	[kg]
m_v	Spool mass	[kg]
N	Number of windings	[-]

R	Effective brake radius	[m]
R_h	Hydraulic resistance	[Ns/m ⁵]
T	Fluid temperature	[K]
T_{br}	Braking torque	[Nm]
U	Negative overlap	[m]
V_{dead}	Dead volume	[m ³]
W	Orifice area gradient	[m]
X	Volumetric percentage of fluid gas content	[%]
x_b	Caliper displacement	[m]
x_p	Piston displacement	[m]
x_v	Spool displacement	[m]
A	Braking torque/ supporting force ratio	[m]
B	Fluid bulk modulus	[Pa]
H	Fluid absolute viscosity	[Ns/m ²]
Θ	Jet angle	[°]
Λ	Magnetic flux	[Wb]
λ_c	Critical flow number	[-]
N	Fluid kinematic viscosity	[m ² /s]
P	Fluid density	[kg/m ³]

II Abbreviations

BOSTrab	Straßenbahn-Bau und Betriebsordnung
DTV	Disc thickness variation
HMI	Human-Machine Interface
IPS	Ideal pressure source
MVB	Multifunction vehicle bus
PPRV	Proportional pressure reducing valve
PWM	Pulse-Width Modulator

1 Introduction

A brake is a device which converts a vehicle kinetic and/or potential energy into other energy forms to attain slower velocities or to ensure its stationary position against unpredicted moves. Brake systems shall satisfy fundamental safety requirements in terms of reliability and repeatability, ensuring uniform and predictable performances, regardless of the variability of their working conditions. /Cru12/

A major source of uncertainty affecting the operation of frictional brakes is the instability of the friction coefficient arising in the pad-rotor contact surface. This parameter is severely influenced by several factors, including the rotor temperature, the disc thickness variation and runout, the relative velocity of the two contact surfaces and the disc wear. /Lee15/

The deviation of the pad-disc friction coefficient from its nominal value results in undesired phenomena such as brake judder and brake fade, leading to vehicle passengers' uneasiness, pronounced wear and longer halting distances. /Mag14/

The current research effort aiming to avoid this phenomenon, privileges a passive "a-priori" approach: the goal of obtaining accuracy and repeatability in the generated braking torque is addressed mainly by means of material investigation and disc-pads design re-evaluation. /Mar14/

Nonetheless, because of the adoption of non-standard materials and components and their layout of open chain system (without any feedback signal assessing their proper operation and no real-time corrective action carried out), this kind of countermeasures might result in higher manufacturing costs and be eventually ineffective in the long term.

Therefore, implementing an active control of the braking torque already embedded in the standardized brake design appears as the most convenient choice to cut costs and concurrently achieve reliable lasting performances.

In the present work, the above-mentioned concept is applied to a hydraulic active brake for tramway vehicles manufactured by the company Hanning & Kahl. Exploiting the features of the multi-domain platform LMS Imagine.Lab Amesim, the open loop system is simulated and validated by performing exemplary load cycles. Emerging criticalities associated to injected disturbances are highlighted and a closed-loop concept is deployed.

The control system proposed in this project is of hydro-mechanical type, ensuring system proper operation even in case of power failures. It relies on the force measured along a supporting pole included in the brake original structure as eligible variable to estimate the effective torque applied to the rotor. /Pet17/

The feedback force and the set force are conveyed at the two opposite ends of a spool valve. The valve spool moves in order to establish force balance, i.e. consistency between the desired torque and the actual one. Connecting alternatively the valve outlet to the pressure supply or to the tank, the valve produces a pressure rise in the hydraulic actuator when the set force exceeds the feedback one, while it generates a pressure drop when the force acting along the support pole results to be larger than the reference signal.

A parametrization of the system is carried out and a sensitivity study is led to deduce general guidelines for the system design. Eventually, the novel brake system is optimized in order to match the system requirements in terms of braking performance consistency and disturbance compensation.

2 Literature review

This chapter provides an outlook about various brake systems currently adopted on railways vehicles. In particular, tramways brake systems are described and their fundamental components highlighted. Eventually, the phenomenon of brake fade is explained and the main remedies proposed in literature are presented.

2.1 Brake systems on railway vehicles

2.1.1 General overview

Braking systems are an essential feature to guarantee safe and reliable performances for all vehicles. /Sha15/ The purpose of a braking action is to fulfill the following requirements:

- Attain a slower velocity;
- Avoid unwanted acceleration along a downhill;
- Allow stop to a fixed point;
- Keep the vehicle in a stationary position when it is halted.

A braking system shall own some fundamental characteristics:

- In an emergency situation, it shall allow to stop within the shortest possible distance;
- No skidding condition shall arise during brake application;
- Effectiveness shall be kept constant even during prolonged application and shall not vary within the entire working life;
- It shall keep the vehicle in a stationary position when the driver is not present.

The braking system of a railway vehicle may be classified according several principles. /Cru12/ Assuming the mean of braking force generation as a sorting criteria, one can define:

- Handbrakes, also known as parking brakes, manually actuated. They generally are not service brakes, i.e. they are not used for braking while operating. They shall prevent any unplanned move while the vehicle is halted.
- Pneumatic brakes, which exploit pressurized air to achieve brake application or release, accordingly. They can be further distinguished in direct pneumatic brakes, which merely

adopt the compressed air as actuating mean, and indirect pneumatic brakes, which feature the pressurized air as control signal too.

- Electro-pneumatic brakes, which use electric command signals, while they perform their braking action through compressed air.
- Rail brakes, which utilize an electric command signal, while the braking action is performed by means of magnetic force induced by large electro-magnets placed under the vehicle's bogie over the top forces of the rail. Since their exerted braking force is independent from the wheel-rail adhesion condition, they are usually employed jointly with a frictional braking force.
- Electric brakes, whose working principle is based on the reversibility of the electric engine, which in this case is used as generator, allowing the kinetic and/or potential energy of the vehicle to be converted into electric one. The dissipated energy is either recovered or dissipated as heat on a rheostat.
- Hydraulic brakes, which make use of hydraulic oil as braking fluid; they can be further distinguished into hydrostatic (the braking action is achieved by applying compressed fluid) and hydrodynamic (the vehicle kinetic energy is converted into heat in a rotor pump and eventually dissipated). This kind of braking system is widely spread on tramway vehicles, where the need for low-floor design solution consistently reduces the space available for installation.

Considering the braking force generating principle, another classification can be derived /Pan97/:

- Friction brakes, which exploit Coulomb friction between surfaces;
- Dynamic brakes, relying on non-frictional phenomena to achieve braking action (electric, hydro-dynamic and eddy currents brakes belong to this category).

According to the possibility of modifying the braking force while operating, a further distinction can be made /Cru12/:

- Tunable brakes, which allow to modulate the braking force both during the application and release phase;
- Non-tunable brakes, which can attain only a specific braking level and allow achieving only complete release (not gradual).

In vehicles equipped with multiple brake systems, hybrid braking action can be achieved by combining pneumatic brake operation with electro-dynamic brake application. In particular, two different operating modes can be distinguished /Bre12/:

- Interlock: in normal operation, the pneumatic brake is inhibited and electro-dynamic brakes are applied. The pneumatic brake becomes active only when electro-dynamic brakes can no longer be applied because of a failure occurrence, so that the minimum deceleration requirements can still be met.
- Blending: the braking operation is achieved by merging the electro-dynamic brakes action with the pneumatic brake contribution. In order to accomplish wear minimization, the use of electro-dynamic brake is prioritized, and only at its full exploitation, the friction brake is additionally switched on. The braking distribution is designed in order not to exceed the maximum adherence condition defined for the wheel-rail contact patch. In **Figure 2-1** an example of blending application is illustrated: motor carriages M1 and M2 are equipped with both electro-pneumatic brakes (EP1 and EP3) and electro-dynamic brakes (ED1, ED2 and ED3, ED4 respectively), while trailer carriage TC features exclusively an electro-pneumatic brake system EP2. The sum of the two generated braking forces is limited by the maximum adherence condition, corresponding to the attainment of the friction coefficient $\mu_{S,Max}$ at the wheel-rail interface.

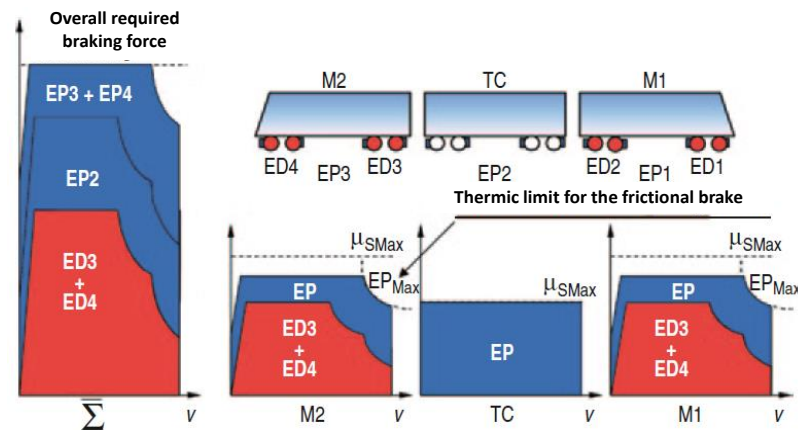


Figure 2-1: Blending and braking force partitioning as a function of the vehicle velocity /Bre12/

A unified parameter to compare the braking capabilities of different rail vehicles equipped with different brake systems is the so-called “braked weight percentage”. The guidelines for its computation in various regimes are defined in /UIC13/. This parameter provides an indication of the train brakes efficiency. It is affected by numerous factors, which are accounted for in its computation: the speed of the brake application, the gradient of the railway line on which the braking action is performed and the braking distance.

Nonetheless, the braked weight percentage only gives information about the average performance of the train in emergency braking and it does not include any safety margin: therefore, it shall be considered as a pure performance indicator rather than a design parameter. In the following paragraphs, the most commonly adopted brake systems for rail vehicles are concisely described, to provide an insight of benefits and criticalities related to each of the mentioned technologies.

2.1.2 Indirect pneumatic brakes

In indirect pneumatic brakes, a pressure drop occurring in a control pipe leads to a pressure buildup within the brake cylinders. The issuing of the brake request signal is decentralized in each bogie by a control valve.

The control valves react on the pressure gradient and derive pressure from the air reservoir in the brake cylinder. The pressure reduction in the control pipe is proportional to the requested braking level: a pressure drop of 3.5 bar (full braking) results in the maximum pressure rise within the brake cylinder, usually 3.8 bar. The brake release is achieved by rising the pressure in the control pipe: also the brake release results to be proportional to the pressure buildup within the pipe. In **Figure 2-2** a representative schematic of the indirect pneumatic brake working principle is reported.

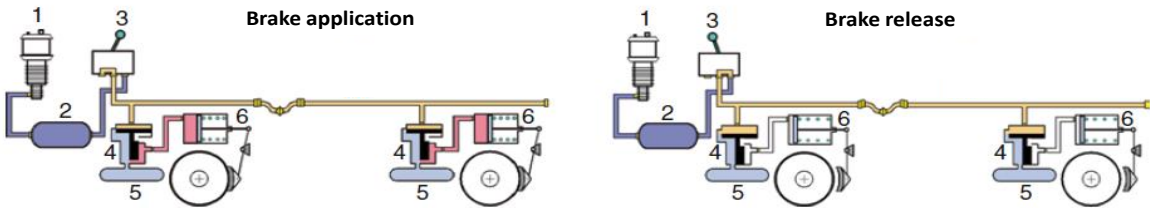


Figure 2-2: Indirect pneumatic brakes working principle schematic /Bre12/. 1. Pressure supply
 2. Air reservoir 3. Brake signal valve 4. Control valve 5. Air supply reservoir 6.
 Brake cylinder

An essential safety feature of indirect pneumatic brakes lies in the independency of each car to the motor bogie, which is responsible solely for issuing of the control signal and not for the actual brake application.

For safety reasons, in order to limit longitudinal forces and prevent shocks, the filling and emptying time of the brake cylinders (thus, the application and release time of braking action) are accurately defined for different vehicle categories by a standard.

According to the halting time one is willing to ensure, different braking regimes can be distinguished: the main distinction which is traditionally operated is the one between “G” trains (adopted for goods transportations, typical of long and slow vehicles) and “P” trains (aimed for passenger transportation, in general faster and lighter). **Table 2-1** defines the typical times for brake application and release on “G” and “P” vehicles.

Braking regime	Time limit for brake application [s]	Time limit for brake release [s]
G	15-20	45-60
P	3-5	18-30

Table 2-1: Time limit for brake application and brake release for rail vehicles of type “G” and “p”

Besides the main categories, further classes can be distinguished (see **Table 2-2**).

Braking regime	Definition
G	Trains intended for goods transportation with operating velocity up to 90 km/h
P	Trains for passengers and goods transportation with operating velocity up to 120 km/h
R	Trains for passengers transportation, with operating velocity above 120 km/h
R+Mg	Trains for passengers transportation equipped with magnetic brakes, with maximum velocity above 140 km/h
R+E, R+H, P+E, P+H	Just for locomotives, where “E” and “H” stand for electrodynamic and hydrodynamic brakes respectively.

Table 2-2: Main braking regimes classification

2.1.3 Direct pneumatic brakes

Locomotives are additionally equipped with direct pneumatic brakes. Their brake cylinder can be pressurized and de-pressurized without the need for an additional control signal. Since compressed air is used on passengers vehicles for multiple purposes (such as for pneumatic suspension, doors and toilets operation), an additional pneumatic line is usually needed to be installed. This line connects the pressure supply to the air reservoir of the locomotive and its pressure is kept in the range of 8.5-10 bar. The main air reservoir is also connected to the air tank of the individual cars, in order to support the function of the main air duct and to accelerate brake application and release time.

2.1.4 Direct electro pneumatic brakes

Electro pneumatic brakes are usually adopted as service brakes on underground vehicles. The brake signal is issued by the driver by means of a human-machine interface (HMI) device and it is transferred to the single vehicles to the individual distributed control units via a control line (for instance, through a PWM signal) or via a serial bus (e.g. the multifunction vehicle bus, MVB)./Bre12/

Each brake control unit regulates and monitors one or multiple electro pneumatic brake units. According to the intended decentralization level, an individual brake control unit can be provided for a single or for multiple bogies. The pressure regulator of each control unit generates a signal proportional to the issued brake request which is converted, by means of a relay valve, in a correspondent pressure rise in the brake cylinder. The individual load-dependent correction of the braking pressure occurs mechanically in the relay valves or is already accounted for in the setpoint definition performed within the brake control units. /Pan97/

In accordance to the fail-safe principle, a pneumatic control pipe is included in the brake system design as back-up solution. An individual load-dependent pressure limiter prevents the potential arising of over-braking condition.

2.1.5 Magnetic brakes

Magnetic brakes are independent of the wheel-rail adhesion force. They can be used as additional brake system. However, the friction between magnets and rails leads to considerable wear. Therefore, they are usually employed in case of emergency braking.

The produced braking force is non-tunable and it increases with increasing vehicle velocity. An excitation power of 1kW produces in a 1 m long magnet a braking force of about 84 kN. /Bre12/ In some cases, the braking action can also be generated by permanent magnets, but their switching can be technically demanding.

2.1.6 Eddy currents brakes

Eddy currents brakes are wear-free and allow to dissipate high power when the vehicle is travelling at high velocities. The magnetic field generated by magnets mounted below the bogie induces circular eddy currents in the rail, which oppose the magnetic excitation field. As a result, the vehicle is decelerated. Compared to magnetic brakes, linear eddy currents brakes don't lead to severe wear effects. Thus, they can be employed in standard operating conditions without any major concern.

2.1.7 Drum brakes

Two main types of frictional brakes can be distinguished: drum brakes and disc brakes. Drum brakes are commonly used on rail vehicles intended for goods transportation and their braking action is performed by means of the application of a brake shoe to the wheel as frictional con-

tact surface. A single brake cylinder can actuate up to 16 brake shoes mounted on 4 different axles, producing a braking force of 48 kN with an average cylinder pressure of 3.8 bar. /Bre12/ In order to compensate the shoes wear and keep the cylinder stroke as constant as possible, slack adjusters are provided. In a confined installation space, brake cylinder, brake shoe, slack adjusters and shoe holder are set in a single block. In Europe, freight cars are commonly equipped with grey cast iron shoes, whose convenient price and well-spread use is counterbalanced by a pronounced corrugation induced on the wheel treads, which results in a noise significantly louder than the one related to other braking systems.

With the purpose of reducing the brake noise, the recent research effort has been focused on the deployment and characterization of organic friction materials. /Bha06/

The friction coefficient of this kind of materials is significantly higher than the grey-cast iron one and less prone to fluctuations. A short-coming of the use of this material relies mainly in the expenses related to the changeover for existing vehicle already equipped with grey cast iron shoes and to the energy partition between shoes and wheels, which is unequally unbalanced towards the latter. /Bre12/ Consequently, wheels are subjected to a more intense thermal stress and they wear off more quickly. On the other side, the operative life of shoes made of organic materials is longer than that of grey iron cast shoes.

2.1.8 Disc brakes

Disc brakes avoid the application of intensive thermal stress to the wheels and allow to accomplish better braking performances with respect to drum brakes. /Rei14/ Considering a unitary axle load of 17.5 t and three discs mounted on each axle, a braking action to standstill starting from a velocity of 350 km/h require an average energy of 28 MJ to be dissipated on each disc. /Bre12/

Wave brake discs are interposed between wheels and wheelsets. It is usual to arrange each wheelset with up to 4 brake discs. On the driving axle, the installation space is severely limited by the presence of the motor drive and gearbox. Therefore, wheel disc brakes are usually adopted. They consist of two friction rings directly mounted on the wheel. Wheel brake disc already provided in two separate spare parts consistently simplifies their replacement, but their design requires care since their splitting point is subjected to heavy centrifugal forces. The clamping force acting on brake disc is applied by brake calipers, which are embedded in

the bogie frame. Compact brake calipers allow a reduction of the required installation space and always include an automatic slack adjustment to compensate wear. In case of emergency braking, clamping forces up to 100 kN may arise.

The most commonly used materials for brake disc are gray cast iron, nodular cast iron, aluminum and cast steel. Gray cast iron is preferred for standard use. When regimes of high thermal stress are involved, aluminum brake discs are preferred, despite their higher cost, because of their high thermal conductivity, which ensures easy cooling capability. If the brake assembly and the trails are specifically designed to withstand high thermal stress, no significant limitation arises from the relatively low melting temperature which characterize aluminum. Cast steel brake disc are preferred when the design process is focused on the durability and on the wear resistance. For operating temperature up to 350 °C, brake pads are manufactured in organic materials. Higher temperatures (up to 800 °C) require pads made from sintered metals. /Bre12/

2.2 Brake systems on tramway vehicles

Trams are operated in crowded and dynamic environment. Because of their high deceleration demands (up to 2.8m/s²) and the reduced installation space, the most commonly adopted braking system on trams are essentially magnetic brakes, electro-dynamic brakes and electro-hydraulic brakes.

2.2.1 Legal requirements

The main legal requirements prescribed in Germany for brake systems mounted on city rail vehicles are collected in the so-called BOSTrab (Straßenbahn-Bau- und Betriebsordnung), the German Federal Regulations on the construction and operation of light rail transit systems, /BOS16/. The standard applies to tramways as well as to light railways and undergrounds. Regulations inherent to the vehicle brake system can be found in Part 5, section 36 of the standard. In clause 1, it is stated that “Vehicles must have at least two brake systems”. /BOS16/ These must be completely independent of each other, so that in case of faults occurring within one of the brake systems, the other system can still be applied; its effectiveness has to be assured also when the contact line voltage fails.

According to this prescription, the majority of city rail vehicles is usually equipped with a frictional brake system, (which envisages the application of pads or shoes against a rotor) in addi-

tion to an electro-magnetic brake system. In particular, the back-up braking solution shall be a fail-safe one, able to guarantee reliable performance even in case of power losses. Thus, hydro-mechanical systems are usually preferred.

Clause 4 of the standard introduces specific requirements for additional brake system: “One of the brake systems must prevent the roll-off of a stationary vehicle with maximum load on the maximum gradient within the system. This brake system has to work as a spring applied system; the braking forces have to be provided and transmitted by mechanical means only.”

/BOS16/

An exception to the previous rules might be allowed only for service vehicles, which do not exceed the velocity of 40 km/h on independent tracks and of 30 km/h on other tracks, which can feature a single brake system.

Anyhow, the designed brake system shall guarantee that a vehicle decelerates to a standstill with a jerk as small as possible and without endangering the passengers and it must fulfil in any operating condition the minimum deceleration requirement listed in **Table 2-3**.

Velocity [km/h]	Deceleration [m/ s ²]	Halting distance [m]
20	0.77	20
30	0.87	40
40	0.95	65
50	1.03	94
60	1.06	131
70	1.07	177
80	1.07	230
90	1.08	290
100	1.09	355

Table 2-3: Minimum deceleration requirements prescribed by BOStrab for light rail vehicle

2.2.2 Design configuration

A frequently adopted configuration envisages the trams motor bogies to be equipped with electromagnetic brakes and spring-applied actuators, while the trailer bogies feature usually hydraulically applied brakes. In order to understand how different braking systems are arranged and

operate on rail vehicles, a schematic of the vehicle Flexity Classic manufactured by the company Hanning & Kahl is shown in **Figure 2-3**.

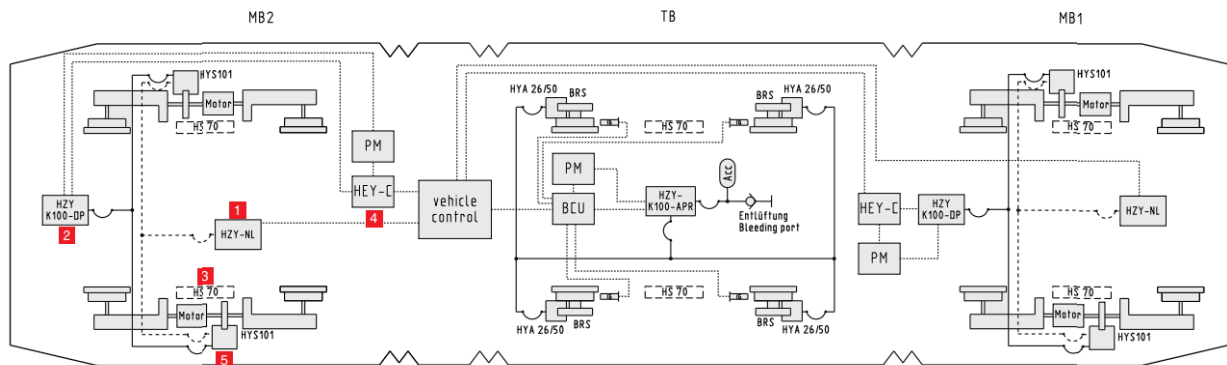


Figure 2-3: Overview of the braking equipment featured by the light rail vehicle Flexity Classic /Han16/

The vehicle consists of two motor bogies and two trailer bogies. The motor bogies are provided with passive brakes, while the trailer bogies are equipped with an active brake caliper on each wheel.

The term “passive brakes” refers to fail-safe actuators which are spring applied and hydraulic released, i.e. the braking action starts when the pressurized oil is no more supplied, for instance when a failure in the hydraulic line occurs. Their working principle is shown in **Figure 2-4**.

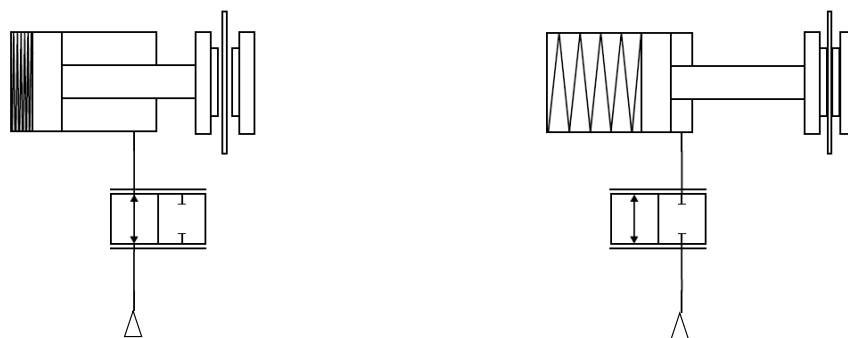


Figure 2-4: A passive fail-safe brake in the released position (on the left) and in the applied position (on the right) /Zak16/

The opposite concept is related to “active brakes”, whose braking action is initiated by the injection of fluid into a hydraulic actuator. A return spring centers the actuator to its rest position resulting in the release of the brake. This principle can be visualized in **Figure 2-5**.

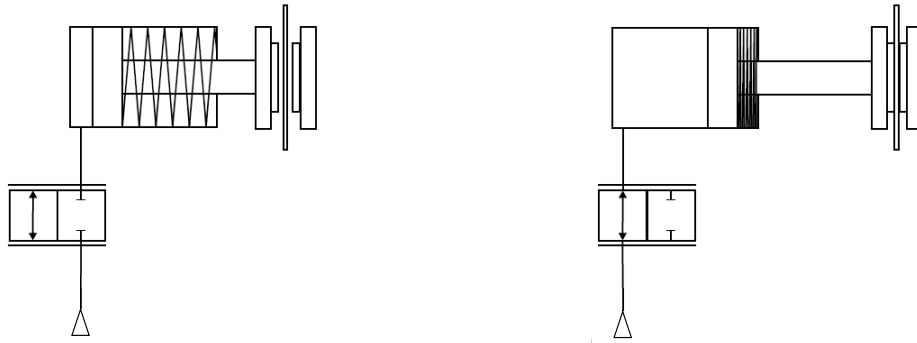


Figure 2-5: Active brake in the released position (on the left) and in the applied position (on the right) /Zak16/

A stepped control is applied to motor bogies by means of a hydraulic power unit, while proportional control is adopted for trailer bogies, exerted by a hydraulic power unit by means of an external pressure accumulator. /Han16/ The brake control unit performs wheel slide protection function in conjunction with wheel speed sensors. The train control unit produces braking commands in accordance with the vehicle weight.

If one of the speed sensors detects a wheel slide, the braking force is either partly or completely reduced for a short time in order to prevent a wheel-lock.

In accordance with BOStrab standard, all bogies are provided with trail brakes which, since act independently of the wheel/rail adhesion. Therefore, they can be used for emergency braking.

2.3 Potential losses of brake effectiveness

Due to the complex phenomena arising in the contact zone of frictional brakes, the effectiveness of the braking performance is not always guaranteed. Multiple factors, e.g. temperature, wear, rotor superficial defects might alter the ideal condition and deviate the system from proper operation. The major phenomena which may affect braking performance are brake fade and brake judder.

2.3.1 Brake fade

The term “brake fade” indicates the phenomenon of degraded braking effectiveness occurring as a consequence of the reduction of the friction coefficient at pad-rotor interface. An exhaustive categorization of the fade phenomenon has been provided by /And90/. Even though Anderson classes refer to automotive brakes, this subdivision allows to define the main factors responsible for this phenomenon. With the previous assumptions, the following categories may be derived.

Blister Fade: The occurrence of this phenomenon is linked with the use of new brake linings which may still contain volatile residuals from the fabrication process, not completely released by the end of the burnish treatment. This would result in high internal pressure rise induced by sudden and intense heating, as during hard brake application. The friction loss is a consequence of the excessive pressure arising at the blister sites and from evolved gases.

Contamination Fade: This kind of phenomenon mainly affects high surface area brake and is induced by water or oil contamination on the surface of the brake lining or brake disc, which generates an elasto-hydrodynamic fluid film which may severely influence the porosity, compliance and wear characteristics of a friction material.

Pad fade: The performing of repeated and intense braking actions might induce extreme temperatures achieved at the pad-disc interface. Sometimes, the pads overheating may lead to melting or to a remarkable change in the material frictional characteristic, resulting in a lubrication effect and hence a friction drop.

2.3.2 Brake judder

By “brake judder” one refers to a braking induced forced vibration, which can occur on a wide range of vehicles. /Dra10/ Since its causes are usually related to disc geometrical defects, its frequency results to be proportional to the rotational wheel speed, hence to the vehicle velocity. According to the factors inducing this phenomenon, a hot or cold brake judder arises. Hot judder originates from thermal deformation, e.g. coning or waving of the disc, while cold judder is linked to geometrical irregularities related to machining, mounting and uneven wear. Nevertheless, this classification might be misleading, since both types usually arise at the same time during the operation. For instance, a high disc thickness variation (DTV) level may induce

an uneven distribution in the contact pressure. Therefore, restricted area will be subjected to extreme high temperatures.

The most common causes of disc brake judder are DTV and disc run-out. In addition to permanent geometrical defects, other temporary irregularities may arise (usually as a result of thermal stress). In brake systems featuring floating calipers, an increase in the clamping force exerted on one rotor side is compensated (at least partially) by a decrease of the normal force applied on the opposite side.

Therefore, deviations from ideal disc geometry, play usually a negligible contribution in originating braking torque variations. Exceptions can be noticed as the phenomenon approaches extreme values when non-linearities and inertia forces play a major role.

Initial DTV results from manufacturing and mounting, but during the operation, the magnitude of this defect is enhanced by numerous phenomena, such as wear and cleaning processes, uneven friction film thickness, uneven corrosion and deposition of heated pad material.

2.3.3 Solutions proposed in literature

As stated in the previous chapter, discrepancies between the ideal and the actual braking torque may occur due to the complex phenomena arising at pad-disc interface. Consequently, the friction coefficient can vary in the contact area and it may affect the system performance, especially on vehicles equipped with wheel-slide protection devices. /Zha10/

Zhang in /Zha10/ highlighted how disc brake unevenness generates both brake pressure variation and braking torque variation which severely affect the performance of an automotive disc brake in terms of wheel stability, braking distance, braking comfort, braking pressure pulsation and vehicle longitudinal oscillations.

Nowadays, the braking torque is generally not subjected to a closed loop control. As a result, phenomena as brake fade and brake judder can't be actively compensated.

Few concepts of closed-loop disc-brake systems have been introduced in recent years. Alternatively, instead of actively controlling the braking torque, the accuracy and the repeatability of the generated braking torque can be achieved passively. For this purpose, the materials of the brake pads and the brake disc are modified to keep the friction coefficient as constant as possi-

ble. For instance, Mitsumoto in /Mit17/ proposed a graphite-titanite alloy as a suitable material for brake pads, which show an elevated temperature lubricity and high thermal conductivity.

Osenin, et al. in /Ose17/ argued that the stability of the friction coefficient at a pad-disc interface shall be guaranteed by using different friction materials arranged according to a force scheme which ensures individual loading on each friction material. However, this alternative approach to the closed-loop control of the braking torque might result in higher manufacturing costs and eventually performance degradation in the long term. Therefore, implementing an active control of the braking torque appears as a convenient choice compared to other solutions.

One of the challenges related to closed-loop control of the braking torque is the choice of a suitable feedback signal. The braking torque can be measured by sensors. However, those sensors are often not suitable for use in rough conditions like the ones characterizing railway applications. Hence, a different physical quantity must be exploited for this purpose. Martinez et al. in /Mar14/ suggested an estimation of the braking out of sensor information, which is available on a standard vehicle. Particularly, their approach is based on an accurate model of the overall braking system including the caliper pressure, wheel speed, and wheel disc temperature. Lee in /Lee13/ proposed an alternative approach for the closed-loop control of the braking torque in automotive applications. He modelled the discrepancy between the set braking torque and the actual one by considering both the error in estimating the friction coefficient and the disc thickness variation, which can be approximated as a harmonic disturbance dependent on the wheel position. One shortcoming of this method is that the need for online wheel position measurements is not available in production vehicles. Thus, a solution without sensors appears to be advantageous compared to a solution with sensors.

Within a research project, which was conducted at the Institute for Fluid Power Drives and Systems (IFAS), a self-energizing hydraulic brake (SEHB) for trains was developed. In 2016, Petry in /Pet16/ introduced a modified concept of the SEHB. He enhanced the required closed-loop control of the braking torque to actively compensate its oscillations. He described the potential and the advantages of a closed-loop brake system compared to an open-loop brake system. In 2017, Petry /Pet17/ proposed a concept of a brake system with a hydro-mechanical closed-loop control of the braking torque. For this purpose, he utilized a force feedback of a support

pole. His study has shown that this feedback signal is directly proportional to the friction force between the brake pads and the brake disc. Moreover, the ratio between the above-mentioned supporting force and the braking torque has experimentally proven to be constant, regardless of the applied torque and the vehicle velocity. Therefore, this force can sensibly be adopted to represent the braking torque in the hydro-mechanical control system.

The results accomplished in /Pet17/ represent the starting point of the study led in this thesis.

3 Analysis of the actual brake system and mathematical model deployment

In the following chapter, the analyzed brake system is outlined. Based on the system description, a mathematical model of the open-loop system is derived. Eventually, a closed control loop concept is presented. This constitute the starting point for the original and novel system simulation and verification, which is conducted afterwards.

3.1 Analysis of the brake system HYA 48/72

Within this thesis, the brake system HYA 48/72 (manufactured by the company Hanning & Kahl) is analyzed (see **Figure 3-1**).

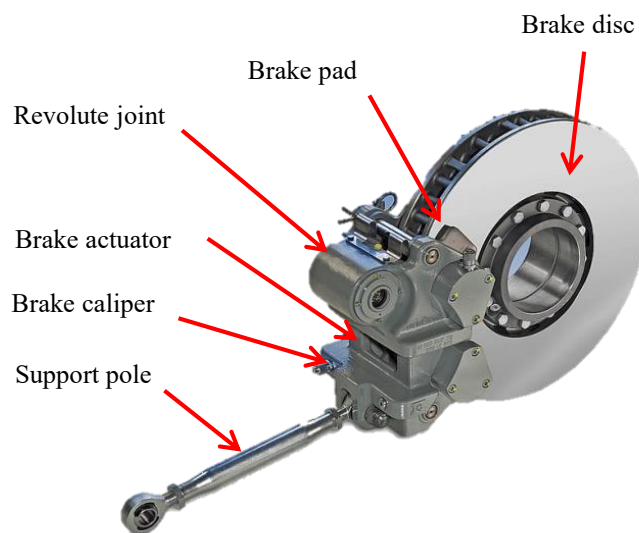


Figure 3-1: Active brake caliper HYA 48/72 by Hanning & Kahl /Han16/

The system consists of a hydraulic active brake caliper of floating type with two hydraulic spring-returned actuators on the piston side. The brake assembly is mounted on trailer bogies by means of a revolute joint and a support pole. It contributes to the braking action provided by electro-dynamic brakes in ordinary operation, while it maximizes the braking action whenever emergency braking is needed.

Because of the compact design and a mechanical interface analogous to the one of spring applied actuators (which are embedded on the motor bogies instead), this brake system fits well in the modular concept and in the reduced installation space which characterize low-floor passen-

ger rail vehicles as tramways. The brake assembly features a one-piece caliper body and two pistons on the inboard side.

The caliper is mounted to this support on two guide pins, which are threaded into the caliper support. The floating caliper working principle can be observed from **Figure 3-2**. The caliper slides on the pin in a sleeve. The pins allow the caliper to move inwards and outwards and provide some flexibility for lateral motion too, in order to ensure its alignment with respect to the rotor position. The pads are attached to the pistons on the inboard side and to the caliper housing on the outboard side. The pistons cross sections and the caliper bore are hydraulic surfaces characterized by the same area. The hydraulic pressure acting against the bottom of the caliper originates a reaction force which moves the caliper body inwards as the pistons move outwards. As a result, the rotor is clamped between the pistons on one side and the caliper body on the opposite side.

As the braking signal is released, the pressure behind the pistons drops, the seals spring back and retract the pistons. As the pistons move back, the caliper relaxes and moves in the opposite direction along the guide pins, to its rest position. The pistons seals provide the self-adjusting action and the required pad to rotor clearance.

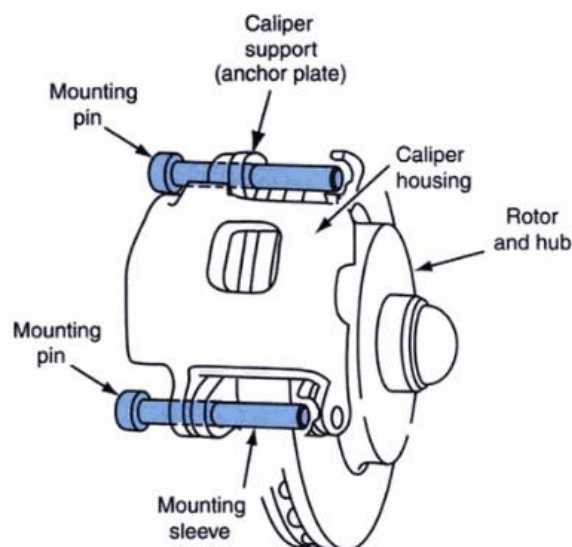


Figure 3-2: Floating caliper fundamental components /Gil05/

The maximum generated clamping force on the disc interface is 72 kN and it is linearly dependent on the pressure at the input port of the hydraulic actuator. The input pressure/clamping

force characteristic of the actuator is highlighted in **Figure 3-3**. P1 and F1 represent respectively the maximum input pressure to the hydraulic actuator (namely, 92 bar) and the maximum clamping force the hydraulic actuator can generate (i.e., 72 kN). Frictional phenomena occurring within the actuator are of negligible entity, therefore no hysteresis cycle can be observed.

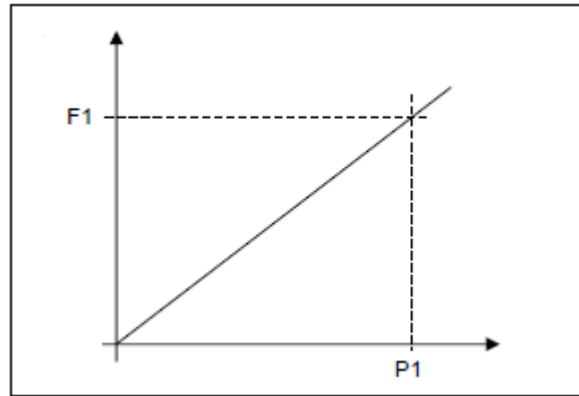


Figure 3-3: Clamping force/input pressure characteristic of the hydraulic actuator (Courtesy of Hanning&Kahl)

The pistons are thermally insulated in order to prevent consistent brake fluid viscosity variation as a result of temperature change. The admissible temperature spans from -20°C to $+60^{\circ}\text{C}$. The maximum achievable braking torque is applied within 300 ms.

The caliper is made up by EN-GJS-400-18C-LT, a ductile iron produced by continuous casting with subsequent heat treatment (ferritic annealing). The material has low hardness, very high fracture elongation and good machinability. The addition “LT” (low temperature) guarantees a minimal value of V-notch impact toughness at -20°C . /ACO16/

The pads material is known as JURID 809. It is a non-asbestos synthetic rubber and resin bonded friction material with metal admixtures, specifically intended for the use on urban rail vehicles. It is characterized by a rated friction coefficient of 0.35. Its mechanical properties, physical characteristics and its operating range are reported in **Table 3-1**.

Characteristic	Value	Unit
Maximum applicable velocity	160	[km/h]
Maximum applicable pressure	160	[N/ cm ²]
Maximum temperature for a prolonged exposition	400	[°C]

Maximum temperature for an instantaneous exposition	500	[°C]
Nominal friction coefficient μ	0.35	[-]
Density	2.60	[g/ cm ³]
Hardness	40	[MPa]
Thermal conductivity	0.7	[W/mK]
Specific heat capacity	0.8	[J/gK]
Shear strength according to DIN 53422	1300	[N/ cm ²]

Table 3-1: Mechanical and physical properties and admissible operating range of Jurid 809
(Courtesy of Honeywell)

The brake fluid used in the hydraulic system is Pentopol J 32. It is a special hydraulic oil with excellent low-temperature characteristic, whose viscosity is less affected by temperature variation compared to conventional hydraulic oils. This decrease in temperature sensitivity is achieved by combining high-quality base oils with selected polymer thickeners, providing an acceptable shear stability of the fluid at same time. The balanced additive system provides enhanced wear protection, reduces friction of sliding metal surfaces and effectively prevents aging phenomena. /Pen06/

The very good performing viscosity-temperature characteristic combined with outstanding low temperature properties qualifies this oil for particular use in hydraulic systems operating at very low or extremely varying temperatures. Typical applications of this fluid include hydraulic systems of door closing and platforms lifting. The fluid main characteristics are listed in **Table 3-2**.

	Unit	Value	Method
Appearance		Yellow and clear	DIN10964
Density at 15°C	kg/ m ³	850	DIN EN ISO 12185
Kinematic viscosity	mm ² /s		DIN EN ISO 3104
- At 100 °C		10.1	
- At 40 °C		31	
- At -40 °C		1340	
Viscosity index		341	DIN ISO 2909
Flash point (Pensky-	°C	113	DIN EN ISO 2719

Martens)			
Pour point	°C	<-60	ISO3016

Table 3-2: Fluid properties of Pentopol J32 (Courtesy of Pentosin)

The brake fluid is supplied from a hydraulic power unit HZY-K140-APR. This compact device consists of three parts: a tank, a manifold and a hood. Its equivalent hydraulic circuit is depicted in **Figure 3-4**.

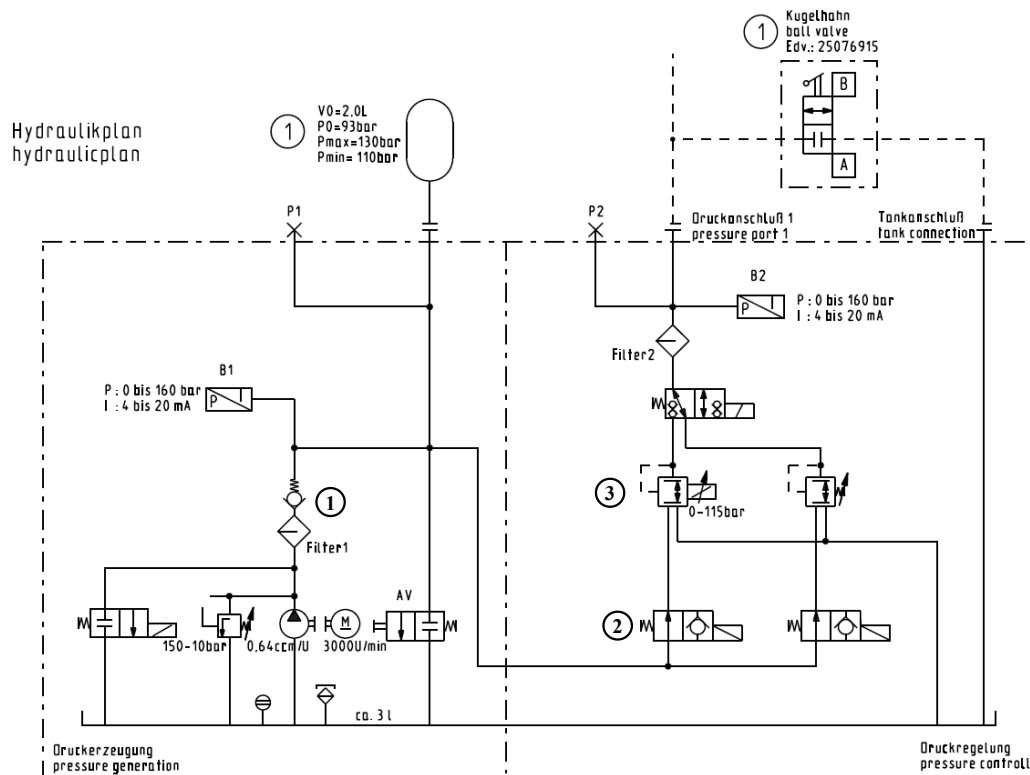


Figure 3-4: Hydraulic circuit of the hydraulic power unit HZY-K140-APR (Courtesy of Haning & Kahl).

As the blocks highlighted in the figure above suggest, the equivalent hydraulic circuit can be ideally partitioned in two different stages: the pressure generation stage and the pressure control stage. The former includes a pump driven by an electric motor and a pressure limiter which prevents the system to exceed the maximum admissible pressure of 150 bar. A spring-loaded check valve (1) inhibits the fluid from flowing in reverse direction and a hydraulic accumulator smooths out pressure pulsation and ensure prompt response time to the pressure demand exerted by the control block.

A normally open valve (2) allows to connect the first stage to the pressure control stage, whose main component is the solenoid driven proportional pressure reducing valve (3). By issuing an electric signal, it allows to modulate the produced braking torque by controlling the valve output pressure.

A disc in nodular cast iron concludes the list of components included in the described brake assembly. The disc ventilation allows to achieve a faster and more effective heat dissipation, while the adopted material is particularly suitable to withstand wear and fatigue.

3.2 Mathematical model of the open loop brake system

The mathematical model of the brake system has been derived according to the simplified schematic displayed in **Figure 3-5**.

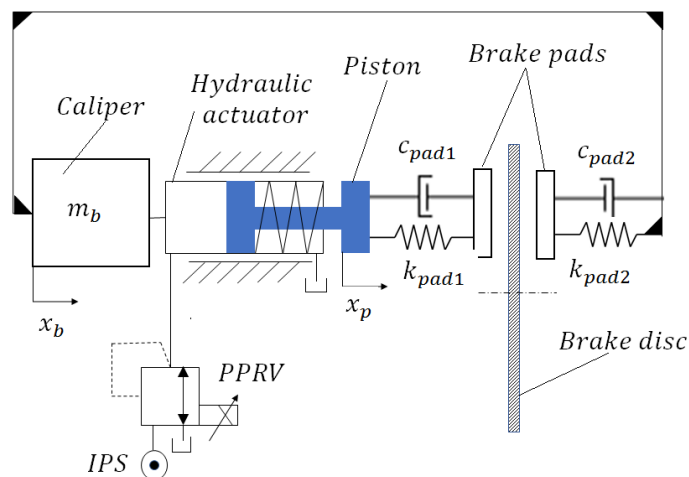


Figure 3-5: Schematic of the simplified braking system

The representation of the hydraulic circuit features an ideal pressure source (IPS) and a solenoid driven proportional pressure reducing valve (PPRV), which is connected through a pipeline to the hydraulic actuator. The model includes a single spring-returned brake actuator, whose cross section was modelled twice as large as the original cross section of the single piston in the actual system. Since the brake is of floating-caliper type, two generalized coordinates, x_p and x_b , have been introduced to indicate the piston and the caliper displacement respectively. Friction relative to caliper and piston displacement has been assumed to be non-zero and a linear model for the return spring has been assumed. Pads masses have been considered to be negligible and their

damping and stiffness characteristics have been described as constant, thus not affected by load and temperature variation.

In the following paragraphs each of the components illustrated in **Figure 3-5** are thoroughly described, the simplifying assumption related to its model is explicitly stated and eventually the mathematical equations inherent to its operation will be derived.

3.2.1 Proportional pressure reducing valve

First, the PPRV is analyzed. The PPRV operated in the system is direct operated. Its purpose is to ensure a downstream pressure proportional to the electric-generated braking signal, regardless of pressure fluctuations in the main circuit upstream.

This goal is fulfilled by balancing the input force and the hydraulic feedback force (representative of the load pressure) acting on the two opposite ends of a reducing pressure control pin, connecting the valve outlet to the pressure supply or to the tank accordingly. A representation of the valve working principle is provided in **Figure 3-6**.

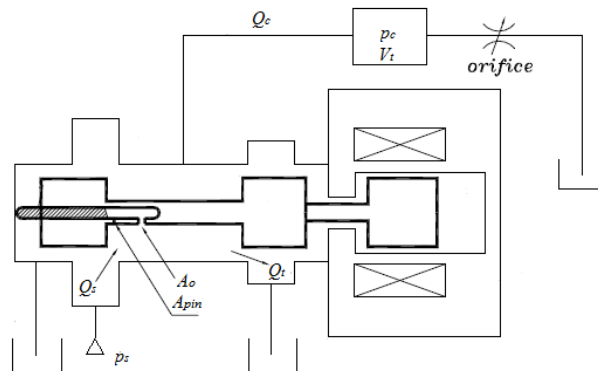


Figure 3-6: Schematic of a direct operated pressure reducing valve /Yun10/

A detailed analytical model of the PPRV can be found in /Yun10/. For the simulation, a simplified representation has been chosen, consisting of a 1st order lag and a hydraulic orifice. The 1st order lag allows taking into account the delay related to the actuation electric constant. Since the 1st order delay element receives a pressure signal as input (representative of the IPS), its output can be computed according to **eq.3-1**:

$$p(t) = p_s \cdot e^{-t/\tau} \quad \text{eq. 3-1}$$

with p_s the supply pressure and τ the time constant of the 1st order delay.

No geometrical information was available regarding the orifice parametrization. Therefore, an equivalent orifice area is estimated from the valve pressure drop/flow rate characteristic defined at atmospheric pressure. The orifice equivalent area is expressed in **eq.3-2**:

$$Q = A_o \cdot c_{q\max} \cdot \sqrt{\frac{2 \cdot \Delta p}{\rho}} \cdot \tanh \left(\frac{2 \cdot D_H \cdot \sqrt{\frac{2 \cdot \Delta p}{\rho}}}{\nu \cdot \lambda_c} \right) \quad \text{eq. 3-2}$$

With Q and Δp respectively the valve flow rate and pressure drop pair defined at atmospheric pressure, A_o the orifice equivalent area, $c_{q\max}$ the maximum flow coefficient, ρ the fluid density, ν the kinematic viscosity of the hydraulic fluid, D_H the hydraulic diameter and λ_c the critical flow number. The hydraulic diameter can be expressed as a function of the orifice area as in **eq.3-3**.

$$D_H = 2 \cdot \sqrt{\frac{A_o}{\pi}} \quad \text{eq. 3-3}$$

Once the orifice area is known, the flow rate Q is obtained from **eq.3-4**.

$$Q = c_q \cdot A_o \cdot \sqrt{\frac{2 \cdot |\Delta p|}{\rho}} \cdot \frac{\rho}{\rho(0)} \cdot \text{sign}(\Delta p) \quad \text{eq. 3-4}$$

The flow coefficient c_q in the previous expression, is computed according **eq.3-5**

$$c_q = c_{q\max} \cdot \tanh \left(\frac{2 \cdot \lambda}{\lambda_{crit}} \right) \quad \text{eq. 3-5}$$

with the flow number λ which can be derived from **eq.3-6**.

$$\lambda = \frac{D_H}{\nu} \cdot \sqrt{\frac{2 \cdot |\Delta p|}{\rho}} \quad \text{eq. 3-6}$$

3.2.2 Pipelines

As long as the pipelines don't exceed a certain length threshold, defined according to /Bea99/ in eq. 3-7:

$$l < \frac{c}{10 \cdot f_{\max}} \quad \text{eq. 3-7}$$

With l the pipeline length, c the sonic velocity in oil and f_{\max} the maximum value of the interesting frequency, the pipeline dynamics can be disregarded and the whole pipeline volume can be added as inefficient volume to the corresponding chamber volume of the cylinder model. Since a relative long connection is inserted between the actuator and the proportional valve, a lumped RC model (see **Figure 3-7**) is assumed for the hydraulic pipe, in order to account for the flexibility of the line walls and the internal line resistance to flow.

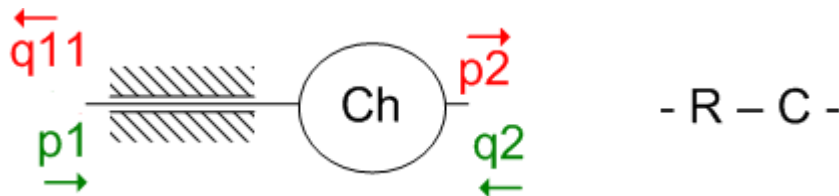


Figure 3-7: RC schematic of the hydraulic line

Considering a volume flow rate Q_r flowing across a hydraulic resistance R_H , referring to the electro-hydraulic analogy, Q_r can be expressed by eq. 3-8.

$$Q_r = \frac{p_1 - p_2}{R_H} \quad \text{eq. 3-8}$$

The pressure build-up in the hydraulic accumulator is dependent of the hydraulic capacitance of the accumulator C_H and on the volume flowrate Q_c according to eq.3-9:

$$Q_c = \frac{p_1 - p_2}{R_H} \quad \text{eq. 3-9}$$

Since the hydraulic resistance and the capacitance result to be connected in a series as highlighted in **Figure 3-7**, $Q_c = Q_r$, thus merging eq.3-8 and eq.3-9, eq.3-10 can be obtained:

$$p_1 = R_H \cdot C_H \cdot \dot{p}_2 + p_2 \quad \text{eq. 3-10}$$

The factor $R_H \cdot C_H$ has the dimension of a time, therefore it is referred to as hydraulic time constant T_H . From **eq.3-10**, it is evident that this model describes a dynamic behavior analogous to the one of a 1st order lag. Thus, the dynamic response of pressure p_2 to a step input p_1 emulates the one highlighted in **Figure 3-8**.

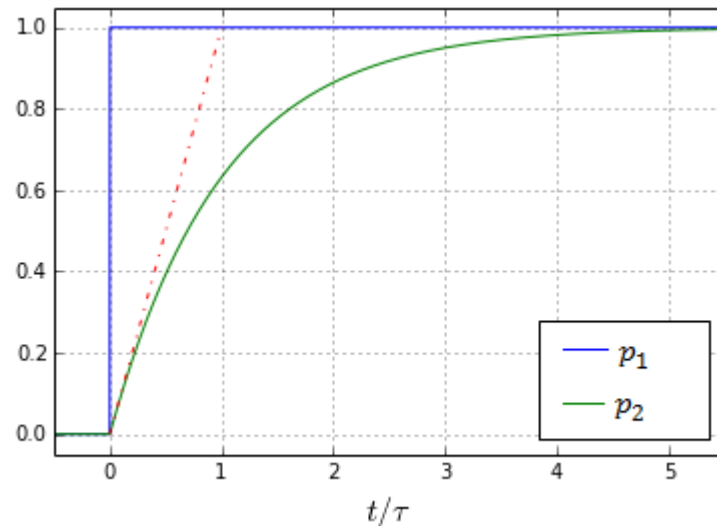


Figure 3-8: Dynamic response of pressure p_2 to a step input change

3.2.3 Hydraulic actuator pressure dynamics

Figure 3-9 shows a sketch of the hydraulic actuator. The brake assembly belongs to floating-caliper class, meaning that the piston body is not fixed. In order to describe the pressure build-up within the actuator it is needed to refer to the piston-body relative displacement. To clarify the meaning of the expressions that are derived afterwards, the piston body and its corresponding generalized coordinates, x_b and x_p , indicating caliper and piston displacements respectively, have been represented too.

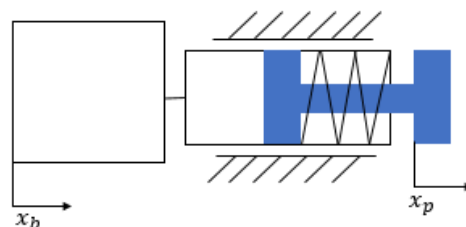


Figure 3-9: Hydraulic actuator simplified representation

Multiple nonlinearities affect the cylinder dynamics, e.g.:

- Pressure dependent effective bulk modulus related to the fluid compressibility as well as to the elasticity of mechanical compliance;
- Friction forces opposing the piston velocity.

In particular, the oil compressibility consistently influences the dynamics of hydraulic systems. The fluid elasticity acts like an additional spring in the actuator and therefore, introduces a second-order mass-spring system whose natural frequency significantly limits the bandwidth of any hydraulic system. The damping of the system is usually small and it is related to leakage flows and viscous friction. In the following equations, the chamber leakage is disregarded.

With the assumptions made above, the continuity equation for the piston chamber can be written as in **eq.3-11**

$$Q = \dot{V} + \frac{V}{\beta(p)} \cdot \dot{p} \quad \text{eq. 3-11}$$

with Q the volume flow rate input to the hydraulic actuator, V the volume of the piston chamber, comprehensive of the valve connecting line and of the chamber actual volume, p the pressure within the piston chamber, β the fluid bulk modulus.

The expression of volume V has been stated explicitly in **eq.3-12**:

$$V = V_0 + A_p \cdot (x_p - x_b) \quad \text{eq. 3-12}$$

With V_0 including the pipeline volume and the hydraulic actuator volume, A_p being the piston cross section, x_b and x_p the body and piston displacements respectively. Volume V time derivative can be written according to **eq.3-13**:

$$\dot{V} = A_p \cdot (\dot{x}_p - \dot{x}_b) \quad \text{eq. 3-13}$$

Re-arranging of **eq.3-11** yields to the hydraulic actuator pressure dynamics equation, given in **eq.3-14**:

$$\dot{p} = \frac{1}{C_h} \cdot (Q - A_p \cdot (\dot{x}_p - \dot{x}_b)) \quad \text{eq. 3-14}$$

with the hydraulic compressibility C_h given by **eq.3-15**:

$$C_h = \frac{V_0 + A_p \cdot (x_p - x_b)}{\beta(p)} \quad \text{eq. 3-15}$$

3.2.4 Brake assembly

Referring to the brake assembly schematic shown in **Figure 3-10**, the equations of motion for the floating caliper and for the piston are written in **eq.3-16**, **eq.3-17** respectively.

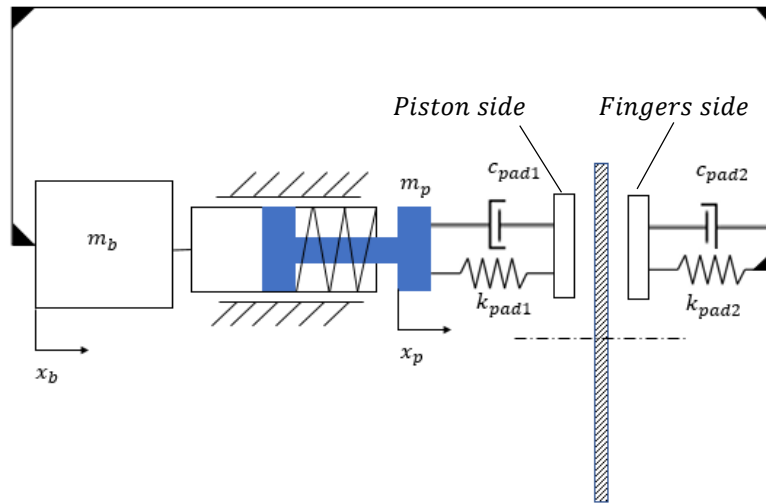


Figure 3-10: Brake assembly schematic

$$m_b \ddot{x}_b = -p \cdot A_p - d_{pb} \cdot (\dot{x}_b - \dot{x}_p) - d_b \cdot \dot{x}_b - k_{spr} (x_b - x_p) - F_{b0} \cdot \text{sign}(\dot{x}_b) - F_{sp0} + F_{N2} \quad \text{eq. 3-16}$$

$$m_p \ddot{x}_p = p \cdot A_p - d_{pb} \cdot (\dot{x}_p - \dot{x}_b) - k_{spr} (x_p - x_b) - F_{p0} \cdot \text{sign}(\dot{x}_p - \dot{x}_b) - F_{sp0} - F_{N1} \quad \text{eq. 3-17}$$

Where m_b and m_p are the caliper and piston mass respectively, d_{pb} is the viscous friction coefficient related to piston-caliper relative displacement, d_b is the viscous friction coefficient between the caliper and the fixed reference frame, k_{spr} is the return spring stiffness, F_{b0} and F_{p0} are caliper and piston stiction, F_{sp0} is the spring preload, F_{N1} and F_{N2} are the clamping forces acting on the piston side and on the fingers side respectively. The Stribeck effect has been neglected.

Clamping forces F_{N1} , F_{N2} are non-linearly dependent of the piston and caliper displacements. Being $x_{b,th}$, $x_{p,th}$ the minimum value of caliper and piston displacements needed to overcome the clearance and hence establish the contact between pads and disc, the expressions for F_{N1} , F_{N2} are stated explicitly in equations **eq.3-18**, **eq.3-19**:

$$F_{N1} = c_{pad1} \cdot \dot{x}_p - k_{pad1} \cdot (x_p - x_{p,th}) \quad \text{if } x_p \geq x_{p,th} \quad \text{eq. 3-18}$$

$$F_{N1} = 0 \quad \text{otherwise}$$

$$F_{N2} = c_{pad2} \cdot \dot{x}_b - k_{pad2} \cdot (x_b - x_{b,th}) \quad \text{if } x_b \geq x_{b,th} \quad \text{eq. 3-19}$$

$$F_{N2} = 0 \quad \text{otherwise}$$

with k_{pad1} , k_{pad2} being the pads stiffness on the piston and fingers sides of the rotor and c_{pad1} , c_{pad2} their damping coefficients.

Naming μ the pad-disc friction coefficient and r the effective brake radius, the braking torque T_{br} acting on the rotor is defined according to **eq. 3-20**:

$$T_{br} = (F_{N1} + F_{N2}) \cdot \mu \cdot r \quad \text{eq. 3-20}$$

Since the mechanical compliance of the axle is assumed negligible, the braking torque is transmitted rigidly from the rotor to the wheel.

3.2.5 Brake fluid

Since the liquid is the medium of power transmission in hydraulic systems, the knowledge of its characteristics is essential to gain a thorough insight of the brake assembly. The most significant fluid properties (i.e. density, viscosity and bulk modulus) have been defined according the Amesim model “elementary fluid with calculated viscosity”. The model mathematical description can be found in /LMS16/.

3.3 Mathematical model of the closed loop system

3.3.1 Closed loop concept description

In the following chapter, the open loop brake system is enhanced by embedding in its design a hydro-mechanical control unit, which fulfils the purpose of accomplishing braking torque consistency, regardless of pad-disc friction coefficient fluctuations. For conciseness reasons, only the new components featuring in the extended system are described afterwards, with the assumptions and mathematical relations previously stated still valid.

According to Petry /Pet17/ (see also Chapter 2.3.3.), the force F_s acting along the supporting pole of the brake assembly is suitable as a feedback signal to estimate the actual braking torque applied to the brake disc, through the relationship given in **eq.3-21**:

$$T_{br,actual} = F_{s,actual} \cdot \alpha \quad \text{eq. 3-21}$$

The hydro-mechanical control mechanism is based on the concept of the mechanical balance of the forces acting on the opposite sides of a spool valve. A reference signal, computed as in **eq.3-22**:

$$F_{s,set} = \frac{T_{br,set}}{\alpha} \quad \text{eq. 3-22}$$

is applied to one of the valve's end, while the force $F_{s,actual}$ is fed to the opposite end of the valve. If no unbalance arises between the two forces (i.e., $T_{br,set} \equiv T_{br,actual}$) the valve spool does not move, therefore the valve remains in its rest position.

If $F_{s,set} > F_{s,actual}$, the valve spool slides, allowing the connection between the pressure supply and the output port, which results in a pressure rise within the hydraulic actuator. If $F_{s,set} < F_{s,actual}$, the valve spool moves in order to connect the output port to the tank, decreasing the pressure of the hydraulic actuator, hence reducing the torque applied to the brake disc. As an equilibrium is restored, the spring allows the spool to return to its initial position. The concept is depicted in **Figure 3-11**.

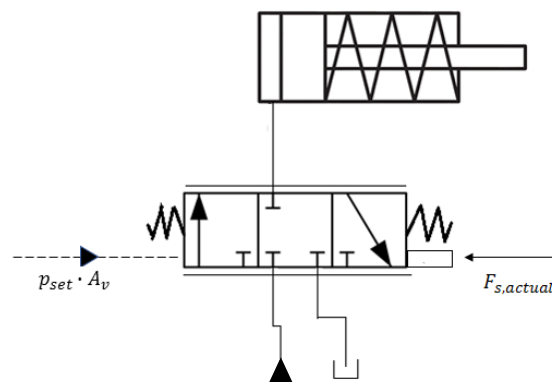


Figure 3-11: Closed loop concept schematic

In the following chapters, equations defining the mathematical model of the control unit are derived. The many nonlinearities arising in the system description are highlighted and, after-

wards a simplified linear model is presented to allow the application of the stability criteria defined for linear components and further on to analyze the closed loop system frequency response. On the basis of this concept, a first parametrization of the control unit is obtained, and sensitivity study is carried out to assess the influence exerted by each of the system parameters on the system dynamic behavior. The results of this analysis allow to optimize the valve design in order to match the system performance requirements.

3.3.2 Spool dynamics

The differential equation relative to the spool motion is written in **eq.3-23**.

$$m_v \ddot{x}_v = F_{s,set} - d \cdot \dot{x}_v - k_{sp} \cdot x_v - F_c - F_{fl} - F_{s,actual} \quad \text{eq. 3-23}$$

By stating explicitly the expression for the reference signal $F_{s,set}$, one obtains **eq.3-24**:

$$m_v \ddot{x}_v = p_{s,set} \cdot A_v - d \cdot \dot{x}_v - k_{sp} \cdot x_v - F_c - F_{fl} - F_{s,actual} \quad \text{eq. 3-24}$$

with m_v the spool mass, x_v the spool displacement, $F_{s,set}$ the reference signal, i.e. the supporting force that would be sensed if the theoretical braking torque was applied to disc, $p_{s,set}$ the pressure needed, given the valve cross section, to generate the reference signal $F_{s,set}$, A_v the valve cross section, c the viscous friction coefficient, F_{fl} the axial component of the flow force, $F_{s,actual}$ the force acting along the supporting pole, chosen as feedback variable, F_c the Coulomb friction, computed as in **eq.3-25**:

$$F_c = -F_{c0} \cdot \text{sign}(\dot{x}_v) \quad \text{eq. 3-25}$$

3.3.3 Control pressure computation

Although the minimum number of required ports for the control valve would have been three (pressure supply, tank and outlet), a four-way valve (with two outlet orifices) has been preferred. This design allows to achieve a pressure sensitivity twice as large as than the one ensured by a 3-way spool valve and thus, under constant and friction load forces, a static error half of the one related to a 3-ports spool valve, as proved in /Mer67/. For simplicity, a critical center spool valve with matched and symmetrical orifices like the one shown in **Figure 3-12** has been considered.

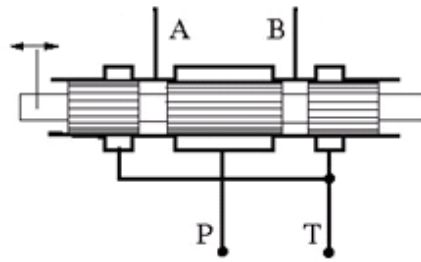


Figure 3-12: 4/2-way spool valve /Mat18/

By applying the electrical analogy, the valve can be equivalently represented as a Wheatstone bridge, as depicted in **Figure 3-13**:

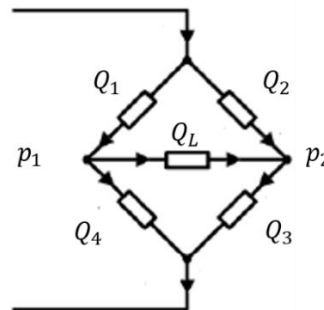


Figure 3-13: Electric equivalent circuit of a 4/2 spool valve /Lun15/

By definition, the pressure drop across the load can be written as in **eq.3-26**:

$$p_l = p_1 - p_2 \tag{eq. 3-26}$$

The volumetric flow rates through the valve port can be described by the orifice equation, reported for each of the 4 valve ports from **eq.3-27** to **eq.3-30**:

$$Q_1 = C_d \cdot A_1 \cdot \sqrt{\frac{2 \cdot (p_s - p_1)}{\rho}} \tag{eq. 3-27}$$

$$Q_2 = C_d \cdot A_2 \cdot \sqrt{\frac{2 \cdot (p_s - p_2)}{\rho}} \tag{eq. 3-28}$$

$$Q_3 = C_d \cdot A_3 \cdot \sqrt{\frac{2 \cdot p_2}{\rho}} \tag{eq. 3-29}$$

$$Q_4 = C_d \cdot A_4 \cdot \sqrt{\frac{2 \cdot p_1}{\rho}} \quad \text{eq. 3-30}$$

The tank pressure has been assumed to be zero, therefore it doesn't appear in the equations above. The orifice areas depend on the valve geometry and they need to be defined as a function of the spool displacement x_v . Assuming matched and symmetrical orifices, **eq.3-31** can be easily derived:

$$A_1 = A_2 = A_3 = A_4 = A_o(x_v) \quad \text{eq. 3-31}$$

From the equations above, one can deduce that if the orifice areas are linear with the stroke (as it usually is), a single parameter shall be defined, i.e. the area gradient w . With matched and symmetrical orifices, the flows in the two diagonally opposite branches of the Wheatstone bridge are identical. Thus, the expressions in **eq.3-32**, **eq.3-33** can be obtained:

$$Q_1 = Q_3 \quad \text{eq. 3-32}$$

$$Q_2 = Q_4 \quad \text{eq. 3-33}$$

Substituting **eq.3-27** and **eq.3-29** in **eq.3-32**, yields to **eq.3-34**:

$$p_s = p_1 + p_2 \quad \text{eq. 3-34}$$

By solving simultaneously **eq.3-34** and **eq.3-26**, **eq.3-35** and **eq.3-36** can be derived:

$$p_1 = \frac{p_s + p_l}{2} \quad \text{eq. 3-35}$$

$$p_2 = \frac{p_s - p_l}{2} \quad \text{eq. 3-36}$$

In order not to over-simplify the valve description, valve leakage has also been taken into account: since the production of an exact zero overlap valve is hardly possible, in reality this kind of valves always display radial clearance and a little underlap.

In non-zero overlap valves (i.e. with non-ideal geometry), the leakage flux dominates their pressure-flow characteristics for small openings, as observable from **Figure 3-14**. Outside this range, the ideal geometry provides a satisfying and reliable description of the system.

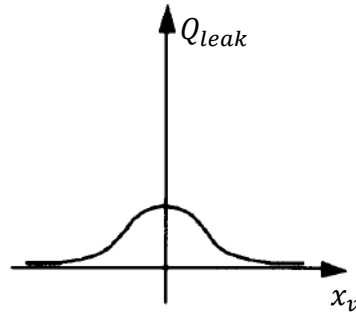


Figure 3-14: Leakage flowrate trend with respect to spool displacement /Moh03/

In order to estimate the magnitude of the leakage flow, Dryden has provided in /Dry56/ a simplified geometric description of the annulus between the spool and the sleeve. Being a the clearance between the spool and the bore, w the bore circumference, l the distance between adjacent grooves machined in the spool, η the fluid absolute viscosity, the leakage volumetric flow rate Q_{leak} can be defined as in **eq.3-37**:

$$Q_{leak} = \frac{w \cdot a^3}{12 \cdot \eta \cdot l} \cdot p_l \quad \text{eq. 3-37}$$

Once volume flowrates Q_1 , Q_2 and Q_{leak} are known from **eq.3-27**, **eq.3-28**, **eq.3-37**, the load pressure dynamic behavior can be eventually described as in **eq.3-38**:

$$\dot{p}_l = \frac{1}{C_h} \cdot (Q_1 - Q_2 - Q_{leak}) \quad \text{eq. 3-38}$$

With the hydraulic capacitance C_h highly non-linear because of the bulk modulus dependency of the fluid temperature and pressure and the control volume being function of the valve spool displacement.

By integrating the load pressure p_l , and recalling the magnitude of the hydraulic actuator cross section and the expressions to define the pad disc-friction μ and the parameter α , the clamping force F_N , the tangential friction force F_T and eventually the supporting force F_s can be easily derived.

3.3.4 System linearization

In order to perform a stability analysis, a preliminary parametrization and a dynamic frequency response study of the system, it is needed to obtain its linearized representation. As it is apparent from the formulae derived in the previous section, the volume flow rates show a dependency from both the pressure drop across the load p_l and the valve spool displacement x_v . To accomplish the intended goal, it is possible to write down for this expression, the Taylor series around a certain operating point, truncated at the first order term, as in **eq.3-39**:

$$Q_l = Q_{l0} + \frac{\partial Q_l}{\partial x_v} \cdot \Delta x_v + \frac{\partial Q_l}{\partial p_l} \cdot \Delta p_l \quad \text{eq. 3-39}$$

The partial derivatives appearing in the relation shown above are usually computed either analytically, by differentiating the equations inherent to the volume flow rate, or graphically from a plot of the curves. From these partials two very important parameters of the valve can be defined.

The flow gain is defined by **eq.3-40**:

$$k_{qx} = \frac{\partial Q_l}{\partial x_v} \quad \text{eq. 3-40}$$

While the pressure-flow gain coincides with **eq.3-41**:

$$k_{qp} = -\frac{\partial Q_l}{\partial p_l} \quad \text{eq. 3-41}$$

The pressure-flow gain has been defined with respect to the negative differential because, since this parameter is always negative for every valve in any operating condition, this expedient would allow the coefficient k_{qp} to be always a positive number.

It might be useful to introduce an additional parameter, k_{px} , i.e. the pressure sensitivity, defined as in **eq.3-42**:

$$k_{px} = -\frac{\partial p_l}{\partial x_v} \quad \text{eq. 3-42}$$

This quantity is related to the above-mentioned parameters according to **eq.3-43**:

$$k_{px} = -\frac{\partial p_l}{\partial x_v} = -\frac{\partial Q_l / \partial x_v}{\partial p_l / \partial x_v} = \frac{k_{qx}}{k_{qp}} \quad \text{eq. 3-43}$$

Therefore, **eq.3-39** is rewritten as in **eq.3-44**:

$$Q_l = Q_{l0} + k_{qx} \cdot \Delta x_v - k_{qp} \cdot \Delta p_l \quad \text{eq. 3-44}$$

The valve coefficients k_{qx} , k_{qp} and k_{px} shall be carefully parametrized in the design phase, since they exert a huge influence on the system stability and on its dynamic behaviour: k_{qx} affects the system open loop gain, k_{qp} influences the valve damping ratio, while k_{px} is directly related to the system steady state error.

Since the system linearization has to be performed about a specific operating point, the choice of this working condition shall also be discussed: the most suitable decision to take is to assume the origin of the pressure-flow curves as reference, therefore for the linearization point is valid $Q_l=p_l=x_v=0$.

For this position, indeed, k_{qx} assumes its maximum value, while k_{qp} has its minimum: with the highest gain and the lowest damping ratio, this point is therefore critical from the stability viewpoint and it can be agreeably stated that if the designed system is stable in this region, it is going to be almost positively stable anywhere.

3.3.5 Closed loop system model summary

A 4 ports, 3 positions spool valve has been chosen to be embedded in the system design to realize the braking torque control. The valve shall be of closed-centre type and be spring-centred. Orifices are supposed to be matched and symmetrical. In order to allow the system linearization, the following analysis is led about the operating point corresponding to $Q_l=p_l=x_v=0$, i.e. the origin of the pressure-flow characteristic. Because of the orifices symmetric arrangement, the lateral component of the flow force is assumed to be compensated. During this early design stage, Coulomb friction has been considered neglectable and only viscous friction has been taken into account.

The dependency of the hydraulic capacitance on pressure, temperature and spool position is in this context disregarded and the parameter is assumed to be constant. Also the pad-disc friction

coefficient μ , the braking torque/supporting force ratio α and the brake radius r are treated as constant value afterwards.

The overall system behaviour can be summarized with the expressions reported from **eq.3-45** to **eq.3-48**:

$$m_v \ddot{x}_v = p_{s,set} \cdot A_v - d \cdot \dot{x}_v - k_{sp} \cdot x_v - F_c - F_{fl} - F_{s,actual} \quad \text{eq. 3-45}$$

$$Q_l = Q_{l0} + k_{qx} \cdot \Delta x_v - k_{qp} \cdot \Delta p_l \quad \text{eq. 3-46}$$

$$p_l = \frac{(Q_l - Q_{leak})}{C_h} \quad \text{eq. 3-47}$$

$$Q_{leak} = k_{leak} \cdot p_l \quad \text{eq. 3-48}$$

Using the relations above, a block diagram of the closed loop system has been obtained (see **Figure 3-15**), in order to evaluate the closed loop transfer function.

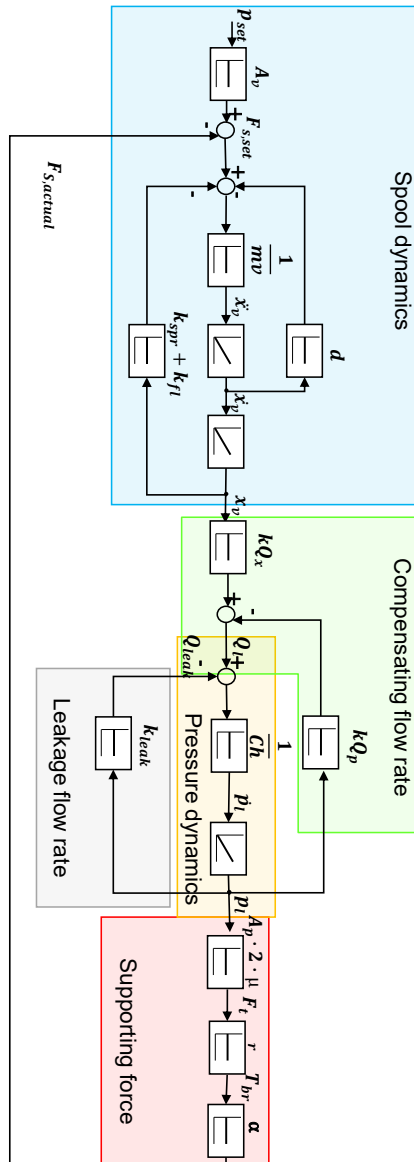


Figure 3-15: Closed loop system block diagram.

By applying the Laplace transform and by using the basics of block diagram algebra, a simplified system sketch can be derived, as shown in **Figure 3-16**:

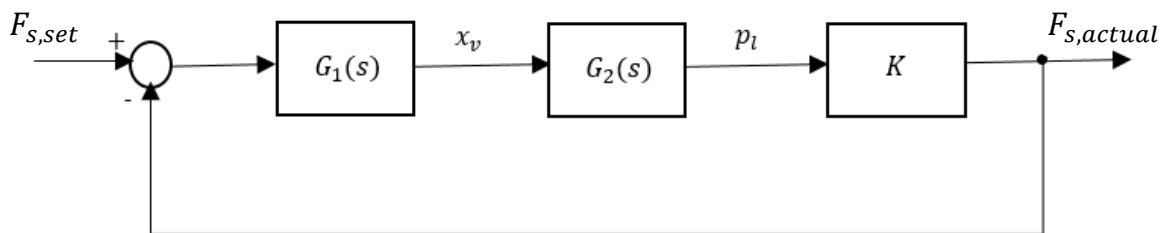


Figure 3-16: Closed loop system block diagram

Given the definitions provided from **eq.3-49** to **eq.3-51**:

$$G_1(s) = \frac{1}{m_v \cdot s^2 + d \cdot s + (k_{sp} + k_{fl})} \quad \text{eq. 3-49}$$

$$G_2(s) = \frac{k_{qx}}{C_h \cdot s + (k_{leak} + k_{qp})} \quad \text{eq. 3-50}$$

$$K = A_p \cdot 2 \cdot \mu \cdot r \cdot \alpha \quad \text{eq. 3-51}$$

The transfer function between the actual supporting force $F_{s,actual}$ and the reference signal $F_{s,set}$ is written in **eq.3-52**:

$$T(s) = \frac{F_{s,actual}(s)}{F_{s,set}(s)} = \frac{G_1(s) \cdot G_2(s) \cdot K}{1 + G_1(s) \cdot G_2(s) \cdot K} \quad \text{eq. 3-52}$$

After carrying out some computations, the expression in **eq.3-53** is obtained for $T(s)$:

$$T(s) = \frac{A_p \cdot 2 \cdot \mu \cdot r \cdot \alpha \cdot k_{qx}}{A \cdot s^3 + B \cdot s^2 + C \cdot s + D} \quad \text{eq. 3-53}$$

The meaning of the factors appearing in the transfer function denominator is stated explicitly from **eq.3-54** to **eq.3-57**:

$$A = C_h \cdot m_v \quad \text{eq. 3-54}$$

$$B = C_h \cdot d + m_v \cdot (k_{leak} + k_{qp}) \quad \text{eq. 3-55}$$

$$C = C_h \cdot (k_{sp} + k_{fl}) + d \cdot (k_{leak} + k_{qp}) \quad \text{eq. 3-56}$$

$$D = [(k_{leak} + k_{qp}) \cdot (k_{sp} + k_{fl}) + k_{qx} \cdot A_p \cdot 2 \cdot \mu \cdot r \cdot \alpha] \quad \text{eq. 3-57}$$

3.3.6 Closed loop system stability considerations

A system is stable when a limited variation of its input variables leads to a limited variation of its output variables. In order to analyze the system stability, it is needed to assess the location of the poles of transfer function $T(s)$: to accomplish this goal, $T(s)$ denominator shall be factorized

and it must be verified that all its roots lie in the right half of the s-plane, i.e. they have a negative real part. It is possible to avoid solving this third order equation by resorting to Routh-Hurwitz test.

According to Hurwitz test, in order to obtain roots having negative real part, it is necessary (but not sufficient) that all coefficients of the analyzed polynomials are positive. If Hurwitz test has been satisfied, Routh test provide the additional criterium to assess the system stability. To perform the test, the “Routh’s array”, made up by the denominator coefficients, shall be built. Routh test assesses that there is one pole in the right-hand s-plane for every sign change of the members in the first column of the Routh array (any sign change is therefore an indication of the system instability). Being $D(s)$ the denominator polynomial, the Routh’s array can be written following the procedure shown from **eq.3-58** to **eq.3-61**: /Oga70/

$$D = a_0 + a_1 \cdot s + a_2 \cdot s^2 + \dots + a_n s^n \tag{eq. 3-58}$$

$$\begin{vmatrix} a_n & a_{n-2} & \dots & 0 \\ a_{n-1} & a_{n-3} & \dots & 0 \\ b_{n-1} & b_{n-3} & \dots & 0 \\ \dots & & & \end{vmatrix} \tag{eq. 3-59}$$

$$b_{n-1} = \frac{-1}{a_{n-1}} \begin{vmatrix} a_n & a_{n-2} \\ a_{n-1} & a_{n-3} \end{vmatrix} \tag{eq. 3-60}$$

$$b_{n-3} = \frac{-1}{a_{n-1}} \begin{vmatrix} a_n & a_{n-4} \\ a_{n-1} & a_{n-5} \end{vmatrix} \tag{eq. 3-61}$$

Since the obtained transfer function denominator is a 3rd order polynomial, the above conditions are equivalent to verify **eq.3-62**:

$$B \cdot C - A \cdot D > 0 \tag{eq. 3-62}$$

Routh-Hurwitz criterion is useful to assess the stability of a system a-posteriori. However, it can’t be used as preliminary design criteria in the analyzed case, because of the parameters in-

terdependency and the abstraction of the denominator coefficients from the physical meaning of the featuring parameters.

Another approach has been utilized: firstly, the physical constraints for the system proper operation have been identified. Then, Matlab/System Control System Tuner has been used to find a first tentative parameter set. Eventually, the valve design parameters have been refined by running an optimization algorithm provided by LMS Amesim within feasible boundaries of the search space. Once the system is parametrized and the open system stability has been checked, the closed loop stability is inquired by performing gain and phase margin analysis. A more detailed insight about the followed procedure is provided in the following chapter.

4 Simulation model and results analysis

4.1 Open loop simulation system

The behaviour of the open loop system and, later on, the control concept for the closed loop one have been simulated on the multidomain platform LMS Amesim. This software package is a suite of tools suitable to model, analyse and predict the behaviour of mechatronics systems, exploiting a wide-range of pre-defined modular components included in a set of thematic libraries.

Based on Bond-Graph theory, the software elaborates a model description by solving nonlinear time-dependent analytical equations that represent the system's hydraulic, pneumatic, thermal, electric or mechanical behaviour. This approach allows to investigate and evaluate the performance of a system even in an early design stage, when the CAD description of the model is not available yet.

Each of the elementary components is associated to an icon and to a set of mathematical equations. The icons shall be connected through ports, which allow power exchange among components. Causality is enforced by linking the inputs of one icon (effort or flow variables, accordingly) to the outputs of another icon.

Each component might be easily customized by setting physical parameters, choosing the sub-model associated to its representation and defining the desired mathematical description among the available ones to characterize the phenomena related to its use (for instance, the friction model for a mechanical component or the viscosity description associated to a hydraulic fluid). Tools aiming to perform system optimization, sensitivity analysis and parameters screening are available as well.

Figure 4-1 gives an overview of the complete open loop simulation model. For visual purpose, the system has been subdivided into different supercomponents, highlighted in distinct colours; each of them is associated to a different stage of the braking process or to a different variable relevant for the braking torque computation.

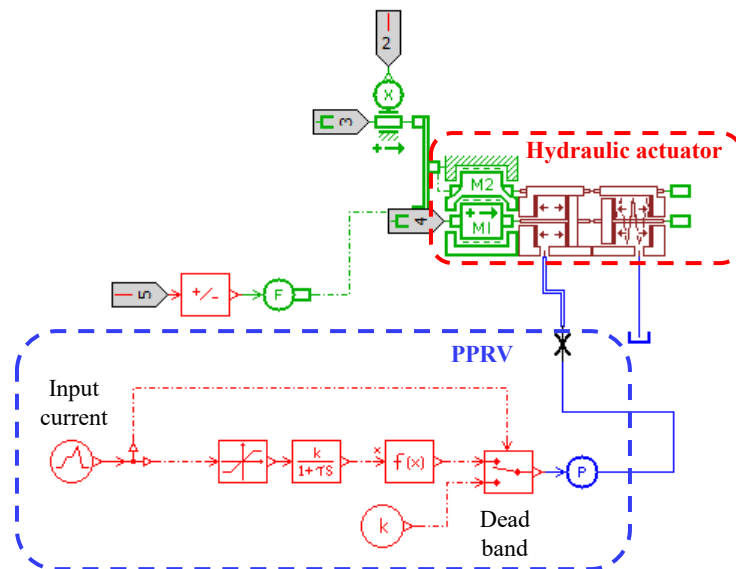


Figure 4-2: Hydraulic components of the simulation model: PPRV, pipeline connection, hydraulic actuator

The PPRV equivalent behaviour has been obtained by combining elements from the signal and from the hydraulic library. The solenoid current, input to the system, has been represented through a piecewise linear source, whose output is split and routed to a saturation block and to a switch: the saturation block limits the maximum input current (hence, the maximum input pressure) within the system working boundaries, while the switch produces an output either equal to zero or linearly dependent on the input variable, according to the value of the solenoid current with respect to the dead band threshold. The 1st order lag takes into account the electric dynamics, while the function block allows the computation of the output pressure corresponding to the current provided. The valve static characteristic was defined by using a hydraulic orifice, for which the hydraulic diameter and the equivalent area were computed given the characteristic volume flow rate and its corresponding pressure drop, specified at atmospheric pressure and for the fluid assumed temperature.

Since the switch block introduced discontinuities difficult to handle for very steep input signal which resulted in undesired spikes in the produced pressure, the system has been simplified by considering exclusively an ideal pressure source, a PT1 element and a hydraulic orifice, as shown in **Figure 4-3**.

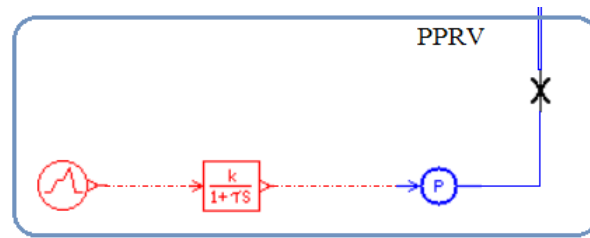


Figure 4-3: Simplified model of the PPRV

For the hydraulic pipeline, a RC model has been selected in order to take into account the fluid resistance and compressibility and the pipes elasticity. The fluid inertia has been neglected. As explained in paragraph 3.2.2, this kind of model introduces an additional 1st order lag in the system dynamics, which can be clearly observed in **Figure 4-4**. Since the hydraulic compressibility of the actuator chamber has been disregarded and the time needed to establish the pads-rotor contact is negligible, the system dynamic behaviour is almost exclusively related to the pipeline connection. The RC model, jointly with the PPRV 1st order lag, produces an overall delay of 300 ms in the actuator pressure build-up with respect to the input signal issuing, which corresponds according to the manufacturer specifications, to the time needed to accomplish the full braking condition.

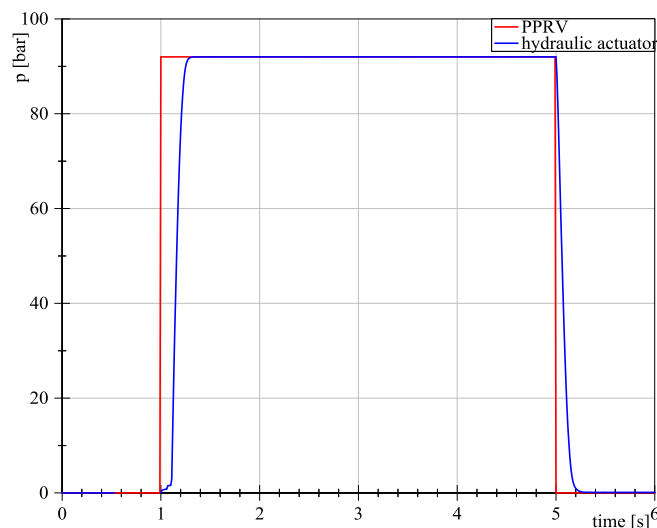


Figure 4-4: Input pressure to the hydraulic actuator (in blue) compared to pressure signal output from PPRV (in red)

Although the original brake is provided with two pistons on the inboard side, a single actuator has been considered in the simulation model. In order to generate the equivalent hydraulic force

produced in the actual system, the piston cross section adopted in the model has twice the individual surface each piston has in the real brake assembly. The hydraulic actuator has been implemented by assembling a mass-envelope module (representative of the piston and caliper masses respectively), a return spring, and a piston with moving body. This was necessary to fulfil the purpose of describing two masses in relative motion, with one of them sliding in the inside of the other, as it occurs in a brake system of floating-caliper type. The data relative to the piston diameter, stroke, return spring stiffness and preload, absolute and relative admissible displacements of caliper and piston masses were deduced from the system datasheet and are displayed in **Table 4-1**.

Parameter	Value	Unit
Piston diameter	70.71	[mm]
Piston stroke	35	[mm]
Piston mass	0.878	[kg]
Caliper mass	37	[kg]
Caliper relative displacements	$x=\pm 3$	[mm]
	$y=\pm 3$	[mm]
	$z=+16;-14$	[mm]
	(max relief /max deflection)	
Return spring stiffness	5.091	[N/mm]
Spring preload	48.37	[N]

Table 4-1: Simulation parameters assumed for the hydraulic actuator model

With respect to friction modelling, the input pressure/clamping force characteristic appears not to be affected by any hysteresis phenomena and the friction acting both on the piston/sleeve interface and between the caliper body and the fixed frame is said to be negligible. However, in order not to over-simplify the system representation, friction has been considered to be non-null. The adopted friction model takes into account both stiction and viscous friction contribution, whose magnitude was evaluated by exploiting the data available for brake system HYS258re, a passive fail-safe spring-applied brake of floating caliper type, manufactured by Hanning & Kahl. Its hysteresis cycle is illustrated in **Figure 4-5**.

With the simplifying assumption of equal friction on both travelling directions, the overall friction (comprehensive of both static and kinetic contribution) has been estimated by considering half of the value of the hysteresis cycle width. In order to distinguish between the static and the kinetic contribution, the condition $F_{br}=0$ has been considered: in this state, the brake actuator is not moving yet, therefore the border of the hysteresis cycle laying on the x axis represents the break-away force needed to apply to the actuator so it can overcome the static friction force and start moving. Given the passive brake cross section and measured on the curve the pressure differential corresponding to this condition, the stiction was computed. By estimating the average piston velocity of the passive actuator, the viscous friction coefficient was evaluated too.

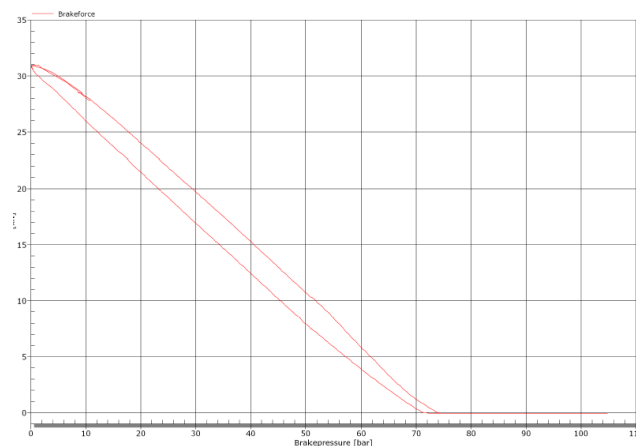


Figure 4-5: Hysteresis cycle for the passive brake HYS258re (courtesy of Hanning&Kahl)

The values of these parameters were then assumed for the active hydraulic actuator. As it is apparent from **Figure 4-6**, no hysteresis is observable in the input pressure/clamping force characteristic of the actuator. A slight deviation from the ideal curve shown in **Figure 3-3** can be attributed to the stiction contribution, even though this behaviour is still fully compatible with the tolerance of ± 1 kN in the clamping force generation prescribed for the actuator by the manufacturer.

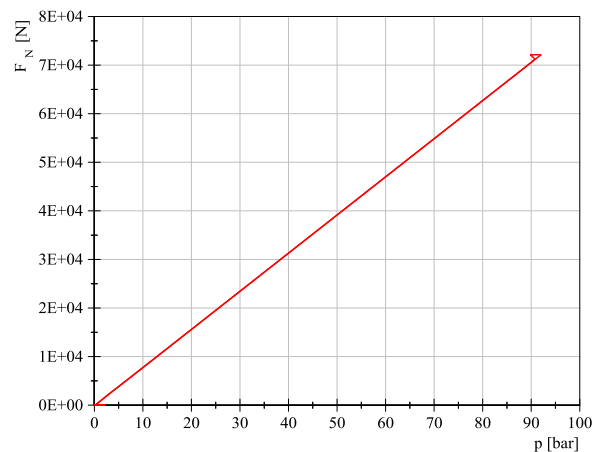


Figure 4-6: Input pressure/Clamping force characteristic of the hydraulic actuator

4.1.2 The elastic contact block: pads-disc interface

The contact between pads and rotor has been simulated by means of an elastic contact module, as shown in **Figure 4-7**. This component implements the contact occurring between two bodies capable of linear motion: in absence of contact, the two bodies move independently from one other, while as the contact takes place a spring and damping force is applied to both bodies. To avoid discontinuities, the value of the damping coefficient varies from zero at first contact to its maximum values as the bodies penetration increases.

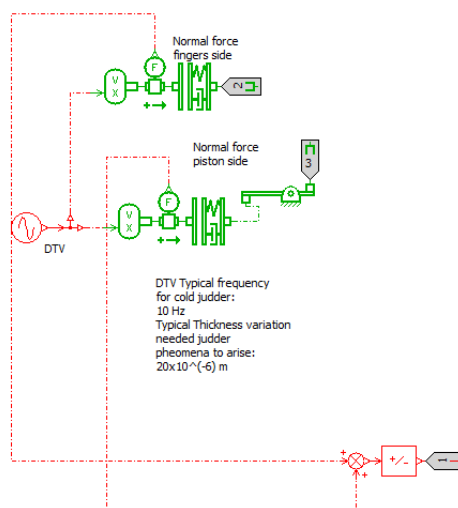


Figure 4-7: Elastic contact modules on rotor piston and fingers sides

In order to evaluate the pads stiffness, the approach suggested by Watany /Wat99/ has been adopted. The pad stiffness k_{pad} , assumed equal on the piston and on the fingers side, has been computed according to **eq.4-1**:

$$k_{pad} = \frac{E \cdot S}{h} \quad \text{eq. 4-1}$$

where E is the pad Young Modulus, S is the pad contact surface and h is the pad thickness. Due to missing information regarding the Young Modulus of the pad material, E was defined according to the procedure described by Gent /Gen12/ from the material indentation hardness. However, this approximation leads to an error range of $\pm 10\%$. The effect of one of the investigated disturbances, i.e. the disc thickness variation, was simulated by feeding to both the contact modules a sinusoidal displacement, which shall represent the effect of superficial roughness and geometrical defects: the disturbance frequency shall be equal to or multiple of the frequency of the wheel rotation, thus directly related to the vehicle velocity, and its amplitude has been set in the range of 10-20 μm , the typical value of rotor superficial unevenness which causes brake judder to arise. As mentioned in chapter 2.3, one of the viable solution for brake judder attenuation is the choice to adopt brake pads made up by materials characterized by a relatively reduced stiffness.

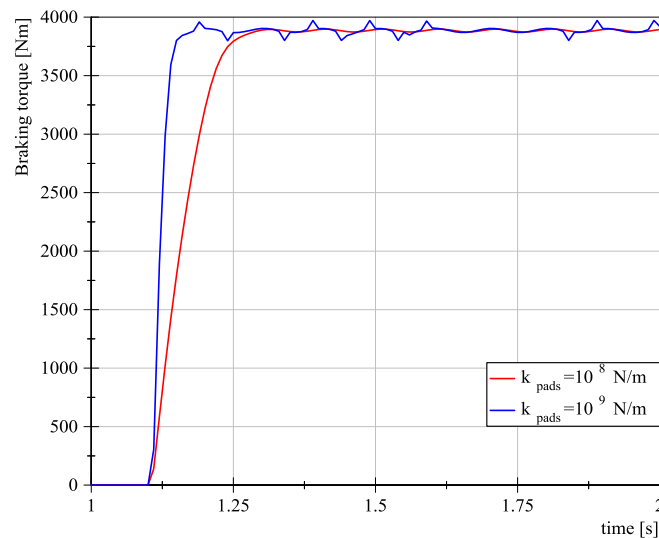


Figure 4-8: Effect of DTV disturbance on the generated braking torque of a system equipped with “soft” pads (in red) and of a system featuring stiff pads (in blue)

As can be clearly observed from **Figure 4-8**, the braking torque generated by a brake system featuring “softer” pads shows smaller oscillations with respect to the braking torque produced by a system equipped with stiffer pads, subjected to an analogous injected disturbance.

4.1.3 The hydraulic fluid

The hydraulic fluid properties are modelled according to the characteristics provided by the manufacturer for the Pentopol J32 in **Table 3-2** and with the oil properties (bulk modulus, density, viscosity) influenced by the operating temperature and pressure conditions. Since no data was available for the fluid bulk modulus, the default value suggested by Amesim settings was assumed.

Even though Pentopol J32 displays a reduced viscosity variation induced by change in temperature, the brake system is characterized by a wide temperature operating range (namely +60° C, -20°C): thus, the impact of viscosity variations on the system braking performances can still be observed neatly.

Figure 4-9 shows the clamping force F_N generated in three different temperature regimes: +15 °C (yellow curve), +60 °C (red curve), -20 °C (blue curve). While the difference in behaviour for the two upper temperatures can be barely appreciated, remarkable is the rising and falling delay that the curve corresponding to the condition $T = -20$ °C shows. Hence, one can reasonably state that at very low temperatures, the resistance opposed by the hydraulic fluid to motion severely affects the promptness of the braking application.

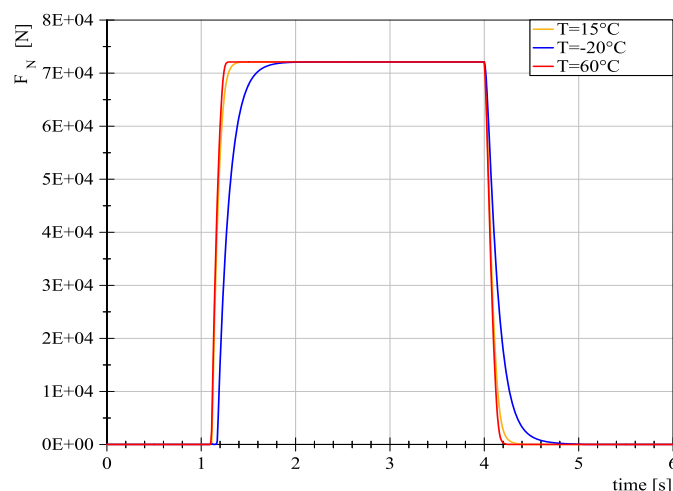
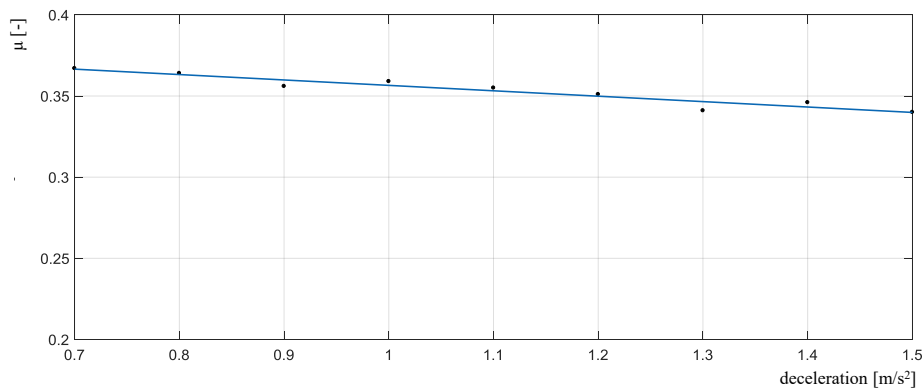
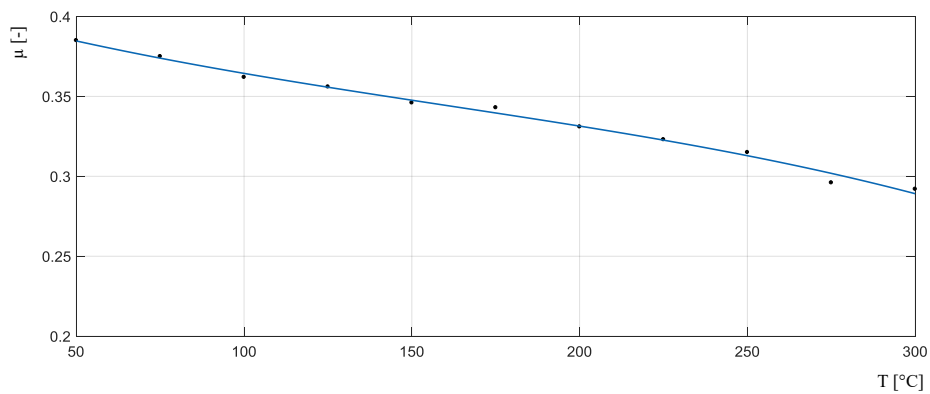


Figure 4-9: Effect of temperature variation on clamping force due to the change of fluid viscosity

4.1.4 Rotor-pad disc friction coefficient

The friction coefficient at the rotor-pad interface is the factor whose excursions affect the most the resulting braking performance. Because of the complex tribological phenomena arising in this contact area, the coefficient cannot be reliably predicted, even if numerous formulae are retraceable in literature. The manufacturer suggested to assume a mean value of $\mu=0.35$ and has provided experimental plots which highlight the distinct contribution of vehicle velocity, acceleration and rotor temperature in determining the value of the friction coefficient. The recorded data have been interpolated by means of Matlab Curve Fitting Tool and approximated as 3rd order polynomial function, obtaining the trends displayed in **Figure 4-10**.



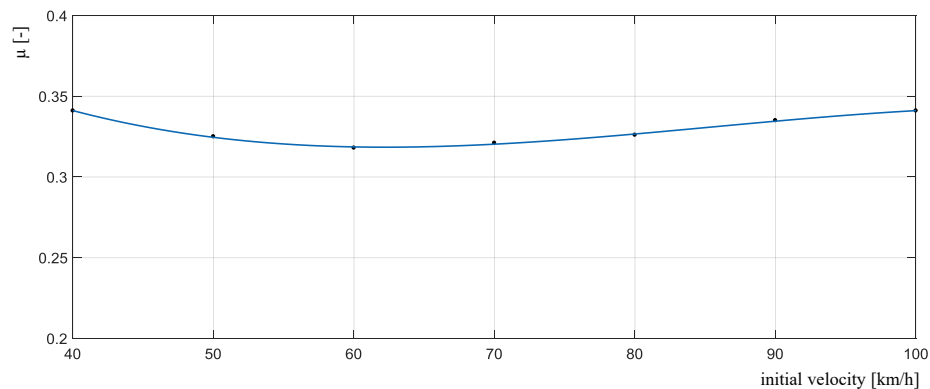


Figure 4-10: Friction coefficient as a function of temperature, deceleration and vehicle velocity variation

The analytical expressions obtained as previously mentioned were implemented in Amesim model by means of the formula block, included in the signal library. Nevertheless, since no indication was available in determining how these three different contributions were actually combined in real operation, their influence could be investigated only independently from each other.

When inquiring the effect on the resultant braking torque of brake fade phenomenon or perturbed rotor-pad contact surface conditions, the friction coefficient was simulated as alternatively as a linear function with negative slope, a sinewave with variable frequency or as a pseudo-random signal, namely a harmonic signal with variable frequency and amplitude.

4.1.5 Brake system kinematic model

The schematic of the brake kinematic model has been shown in **Figure 4-11**. Revolute joints and equivalent distances have been highlighted. For simplifying purpose, the application point of the tangential frictional force to the rotor has been considered located at the pad centre of mass.

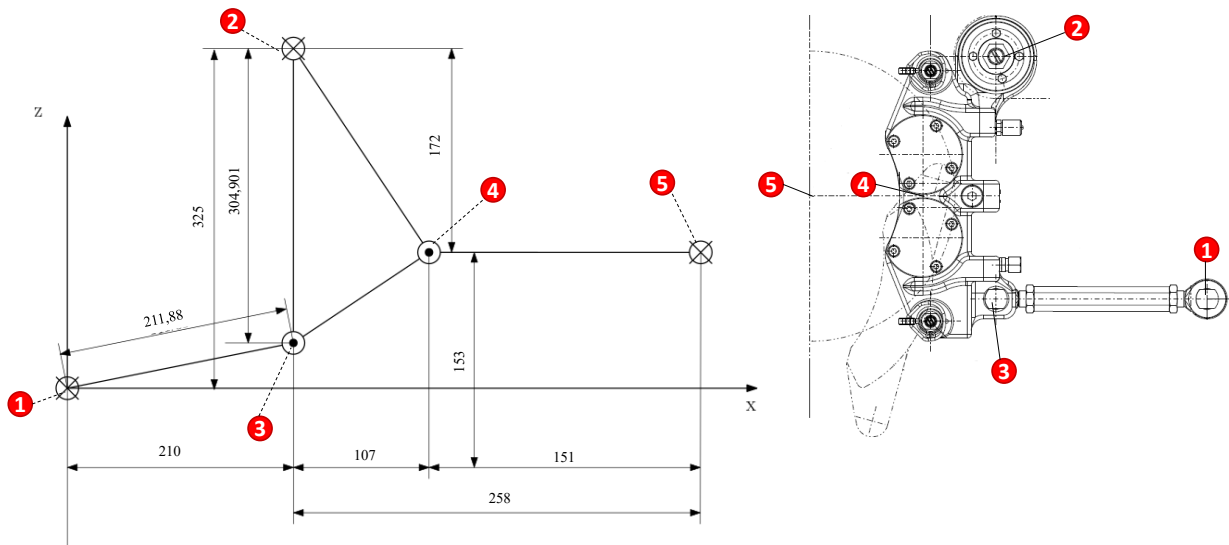


Figure 4-11: Active brake kinematic model

In the simulation model, the brake kinematics has been implementing by using Amesim 3D mechanical library. This choice was made in order not to neglect the brake assembly lateral dynamics, even though no remarkable differences with respect to a planar model were observed. The simulation kinematic block is displayed in **Figure 4-12**.

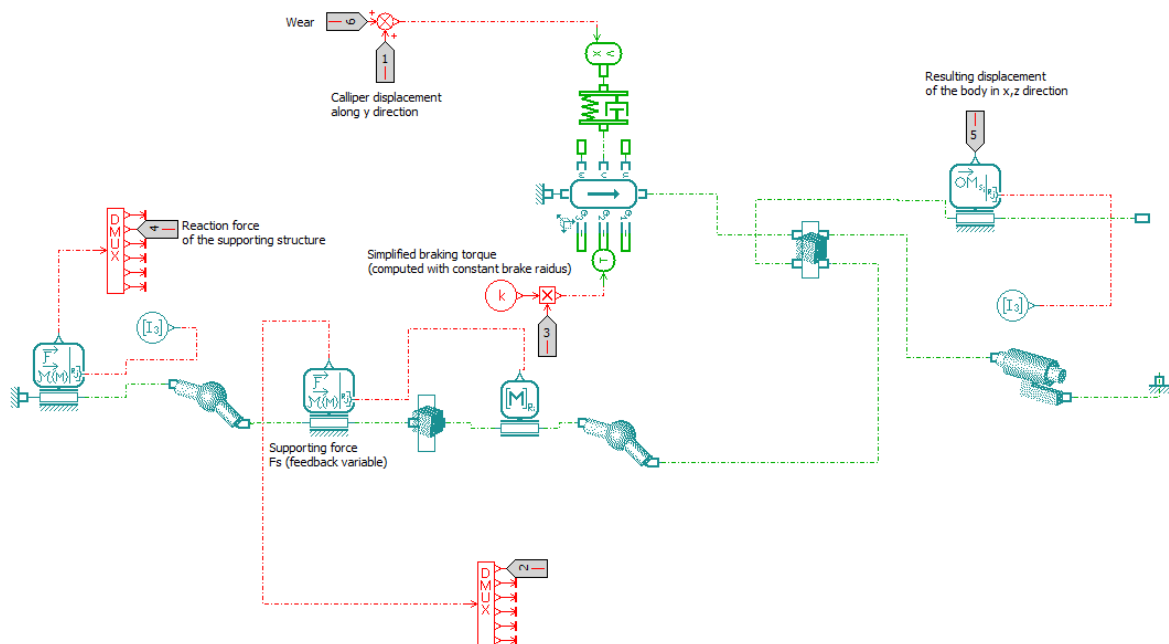


Figure 4-12: Amesim 3D kinematic model

The displacement transducer observable at the top of the schematic allows conveying to the body the displacement occurring along y direction (with respect to the reference frame shown in **Figure 4-11**) resulting from the caliper displacement, consequent to a pressure rise in the hydraulic actuator, and the potential adaption performed by the slack adjuster to cope with the wear effect.

A simplified braking torque (computed with a constant effective radius) has been applied to the caliper body. A force sensor allows monitoring the magnitude of the supporting force F_s acting along the brake supporting pole as a consequence of the brake application. A displacement sensor allows to detect the position variation in the three-dimensional space of the pad centre of gravity, i.e. the application point of the tangential frictional force.

The effective brake radius, which is later multiplied by the tangential frictional force to obtain the braking torque applied to the rotor, has been computed via the components available in the signal library as the distance between the pad centre of gravity and the disc centre, as illustrated in **Figure 4-13**. Even the position of the rotor is not constant but varies in x and z direction (with respect to the reference frame adopted in **Figure 4-11**) as a consequence of the longitudinal dynamics and the suspension travel respectively.

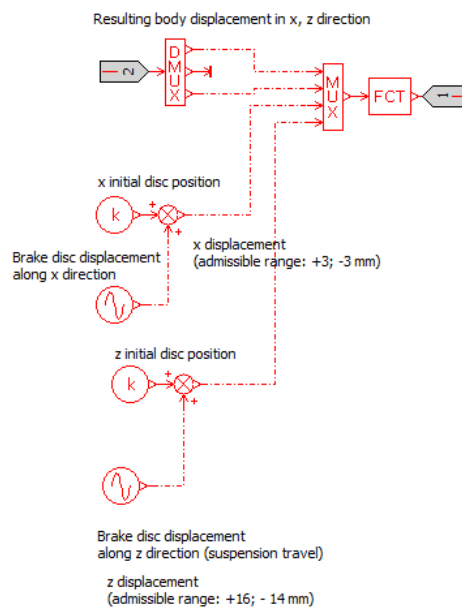


Figure 4-13: Computation of the effective braking radius

4.1.6 Open loop simulation model results

The complete open loop simulation model has been exploited to perform exemplary load cycles both in ideal and perturbed conditions. The main disturbances injected to the model included disc thickness variation, rotor displacement along vertical and longitudinal directions, fade or unevenness in the pad-disc friction coefficient.

One of the assumptions the model was aiming to validate is the premise of the control action intended to be implemented, i.e. the proportionality of the force measured along the brake assembly supporting pole to the braking torque applied to the rotor.

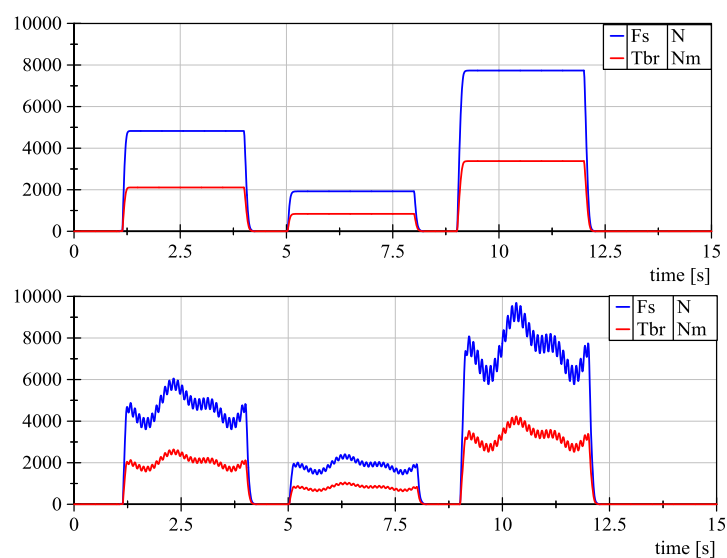


Figure 4-14: F_s and T_{br} relationship for different input pressure and in ideal and perturbed conditions

As highlighted in **Figure 4-14**, the supporting force F_s is proportional to the braking torque applied to the disc regardless of the torque magnitude and to the perturbed conditions. In particular, the coefficient α is affected by the variation of the effective radius occurring as a consequence of the rotor displacement along x and z direction.

Figure 4-15 displays the linear relationship between the braking torque T_{br} and the supporting force F_s , recorded for a series of batch runs performed by allowing a displacement of the rotor theoretical centre along x or z direction accordingly. The first plot corresponds to the condition $\Delta z=0$, $\Delta x \in [+3;-3]$ mm. The slope of the curves, i.e. the angular coefficient of the lines, coincides with parameter α , defined in **eq.4-2**:

$$\alpha = \frac{T_{br}}{F_s} \quad \text{eq. 4-2}$$

For the aforementioned range, α lies in the interval [0.429;0.445], with $\alpha=0.437$ recorded for the condition $\Delta x = \Delta z = 0$. The second plot is obtained by assuming $\Delta x = 0$, $\Delta z \in [-14;+16]$ mm. The slope of the curves, hence the coefficient α varies in the range [0.422;0.453]. Because of these observations, α could be expressed with a 1st order Taylor approximation as in **eq.4-3**:

$$\alpha = \alpha_0 + \left. \frac{\partial \alpha}{\partial x} \right|_{\Delta y = 0} \cdot \Delta x + \left. \frac{\partial \alpha}{\partial y} \right|_{\Delta x = 0} \cdot \Delta y \quad \text{eq. 4-3}$$

Nevertheless, since α excursions in the admissible range of variability for vertical and longitudinal rotor displacements don't exceed the 3.67 % of the value of α_0 , namely the value of α recorded for $\Delta x = \Delta z = 0$, the parameter can be reasonably considered constant and F_s adopted as a suitable feedback signal for the deployed control strategy. In the following analysis, the conditions $\Delta x = 0$, $\Delta z = 0$ for the disc centre has been assumed.

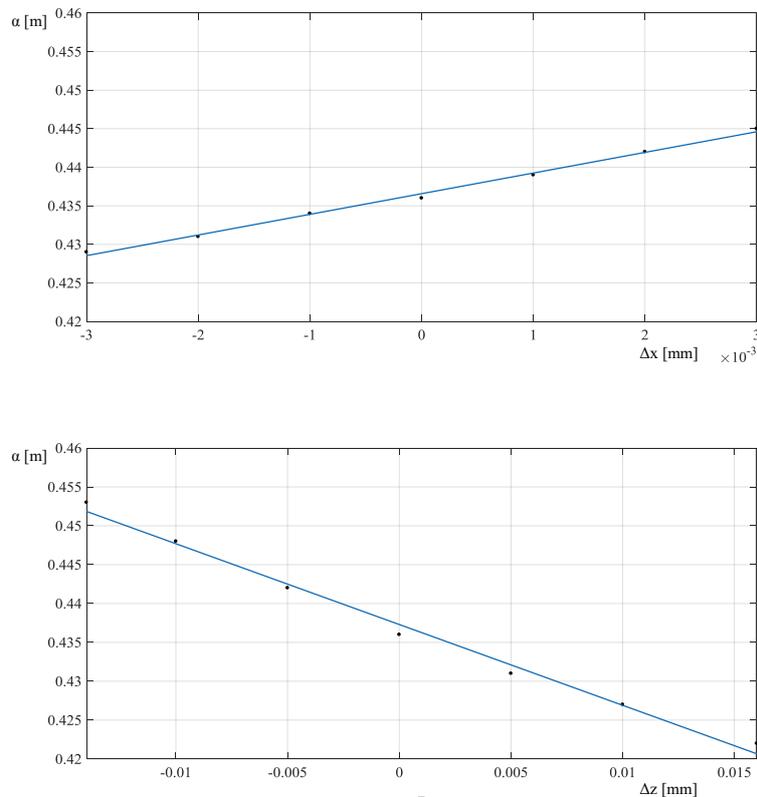


Figure 4-15: α dependency on variable rotor displacements along x and z direction

Figure 4-16 displays the braking torque and the vehicle velocity trend recorded for a simulated load cycle with the pads-rotor friction coefficient respectively considered constant and equal to the rated value suggested by the manufacturer datasheet (i.e., $\mu=0.35$, corresponding to the red curve) and a pseudo-random friction coefficient represented by a harmonic signal, with fundamental frequency equal to 0.5 Hz and mean value equal to 0.35, which allowed to observe the system response to a disturbance varying in amplitude and in frequency.

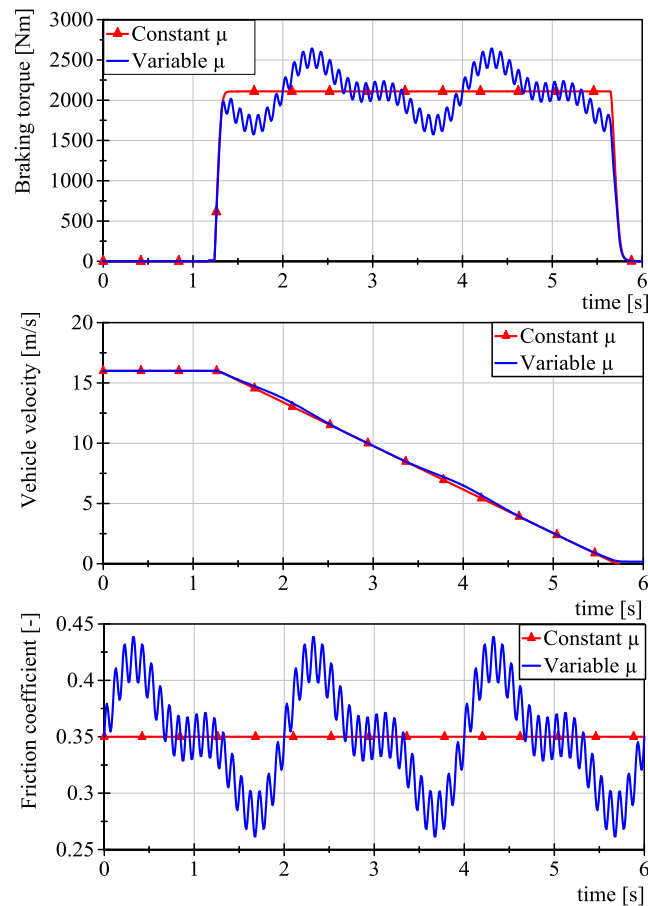


Figure 4-16: Exemplary load cycles simulated for a constant (red curve) and a pseudo-random (blue curve) friction coefficient at disc-pad interface

As it is apparent from the figure above, the braking system is severely affected by the disturbance, with negative peaks of -25.7 % in the generated torque, with respect to the theoretical one, achievable in ideal conditions.

4.2 Closed loop simulation model

In order to pursue the aim of achieving a satisfactory disturbance attenuation, a closed loop simulation model has been developed. The control logic follows the concept already illustrated in the control scheme of **Figure 3-18**. The control valve has been assumed to be of spool type, with zero overlap. Its cross section has been sized so that the hydraulic force generated when the maximum input pressure was applied would equate the maximum supporting force acting along the brake assembly supporting pole, i.e. according to **eq.4-4**:

$$A_v = \frac{F_{s,set_max}}{P_{s,set_max}} \quad \text{eq. 4-4}$$

The hydraulic compressibility C_h of the valve was evaluated according to **eq.4-5**:

$$C_h = \frac{V_{dead} + V_0}{\beta} \quad \text{eq. 4-5}$$

With V_{dead} being the dead volume, comprehensive of the hydraulic pipe connecting the control unit to the hydraulic actuator (a length of 0,5 m and a diameter of 7 mm has been assumed for its sizing) and the dead volume in the hydraulic actuator, V_0 is the volume of brake fluid contained in the cylinder at its end stop, β is the brake fluid bulk modulus. The value of the pressure supply has been set to the maximum brake operating value, i.e. 92 bar. The value of the discharge coefficient was initially established according to **eq.4-6**:

$$B = \alpha_D \cdot \pi \cdot d_v \cdot \sqrt{\frac{2}{\rho}} \quad \text{eq. 4-6}$$

Moderate values were assumed for the spool mass m_v , for the viscous dissipative coefficient d and for the constant K , whose definition is given in **eq.4-7**:

$$K = k_{fl} + k_{spr} \quad \text{eq. 4-7}$$

With k_{fl} being the axial flow force coefficient and k_{spr} the stiffness of the return spring. The valve dynamics was modelled as a 2nd order lag and a natural frequency of 70 Hz and a damping coefficient equal to 1 were assumed. A maximum stroke of the spool of 5 mm was admitted in both directions. According to the direction of the spool motion, the correspondent compensating volume flow rate was generated as in **eq.4-8** or **eq.4-9**, accordingly.

$$Q_l = \sqrt{p_s - p_l} \cdot x_v \cdot B_1 \quad \text{if } x_v > 0 \quad \text{eq. 4-8}$$

$$Q_l = \sqrt{p_l - p_l} \cdot x_v \cdot B_2 \quad \text{if } x_v < 0 \quad \text{eq. 4-9}$$

Since no value for K_{leak} was anyhow retraceable in literature, it was left as “free parameter” to be computed by the design process.

In order to perform an early parametrization of the hydro-mechanical control unit, the overall system behaviour was implemented in Simulink. This choice was made since Amesim doesn't offer a proper tool for control system design: the two main optimization strategies offered by this platform (i.e. the NPQL and the genetic algorithm) can be applied to a wide variety of user-defined objective functions, but because of their extremely heavy computational burden, they require an accurate and extremely limited definition of the search space, in order not to get stuck in local minima and result in unacceptably long run time, leading to no remarkable improvements.

The Control System Tuner available in Simulink enumerates several potential goals to address, defined both in time domain and in the frequency domain according to the user needs. Since this procedure is performed on a linearization of the actual model, it is always necessary to validate the full nonlinear control system with the newfound parameters set. The purpose addressed for the present work was to accomplish the “Step tracking goal”, hence matching the step response from specified input to specified outputs (in this case $F_{s,actual}$) to a target response (namely, $F_{s,set}$).

4.2.1 Closed loop simulation model in Simulink

An overview of the controller realized in Simulink is shown in **Figure 4-17**. The saturation block allows to limit the spool displacement among the predefined end stops. The dead-band block detects negative and positive spool displacements, in order to generate a compensating flow according to eq.4-8, eq.4-9. For simplification purpose, the discharge coefficients B_1 and B_2 have been set to the same value.

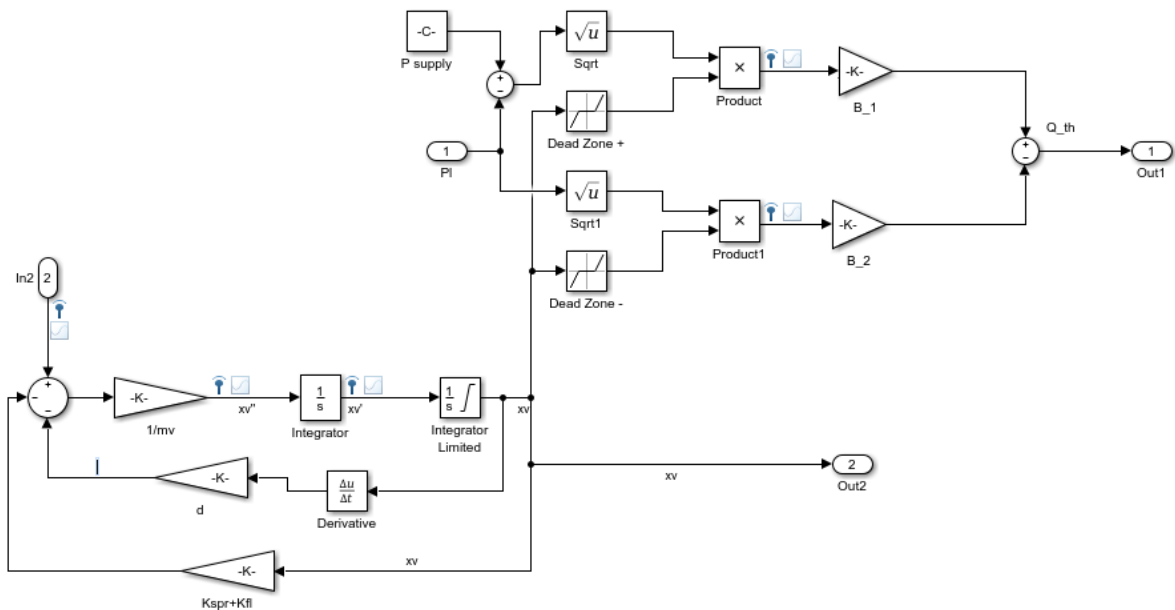


Figure 4-17: Simulink controller logic

The first results obtained with the Control System Tuner suggested value for the leakage coefficient which, even if allowed a close matching with the target response, led to unacceptably high value of the leakage flow rate.

By releasing a further constraint and assuming the discharge coefficient as a “free parameter”, it was observed that in order to obtain a satisfying $F_{s,set}-F_{s,actual}$ tracking response and, at the same time, an acceptable value of the leakage flow rate, a sharp reduction of the discharge coefficient value was needed. As can be understood by recalling the expression for B , stated in eq.4-6, this requirement obstruct the need for a relatively large valve cross-section, necessary to generate the reference signal $F_{s,set}$.

A suitable solution to overcome this ambiguity can be found by equipping the valve with metering edges instead of with standard orifices, to achieve a continuous and sensitive control of the volume flow rate. It was therefore possible to adopt a pair of values for the leakage coefficient k_{leak} and the flow coefficient B which ensured both a satisfying step tracking and acceptable values of the leakage flow rate.

4.2.2 Closed loop simulation model in Amesim

The primitive controller was thus implemented on Amesim simulation model by means of the signal library, in order to test its effectiveness and to refine its parameters set by using the opti-

mization facilities available on the simulation platform. No remarkable difference can be re-traced in the mathematical implementation of the controller logic, as can be observed from **Figure 4-18**.

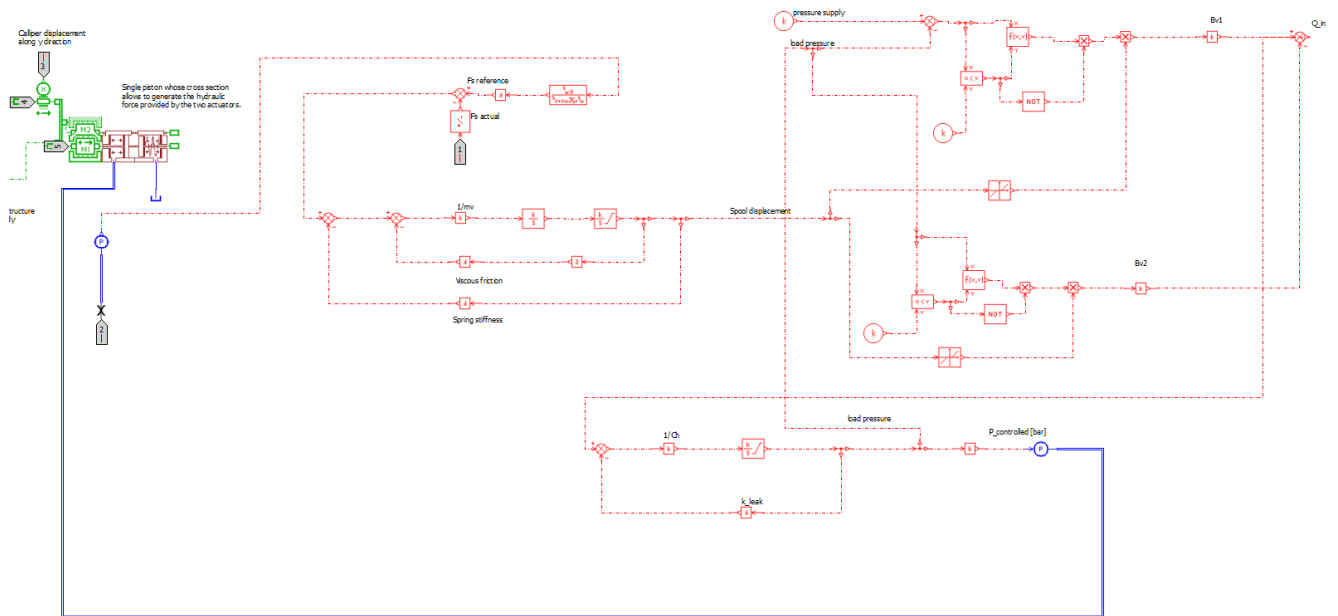


Figure 4-18: Controller logic embedded in Amesim simulation model

The one difficulty to overcome is related to the computation of Q_l according to eq.4-9 at the beginning of the simulation, when the load pressure p_l hasn't been computed yet and its initial value is set to -0; the solver recognizes the computation of the square-root of a negative number as an error and halts the simulation. A series of logic conditions have been enforced to achieve a working running: as shown in **Figure 4-19**. The expression "sqrt(x+y)" has been entered into the formula block, being x the corresponding pressure drop and y an additional variable, added to overcome the simulation error. The value of x, i.e. the pressure drop, is firstly compared to the constant k, whose value has been set to 0: if x results to be bigger than k, the output of the comparison block is 0 (because the condition $x < y$ hasn't been verified). Thus, the computation of the square root of the pressure drop is performed correctly and with no modifications (y would be null, hence would play no role in the expression computation).

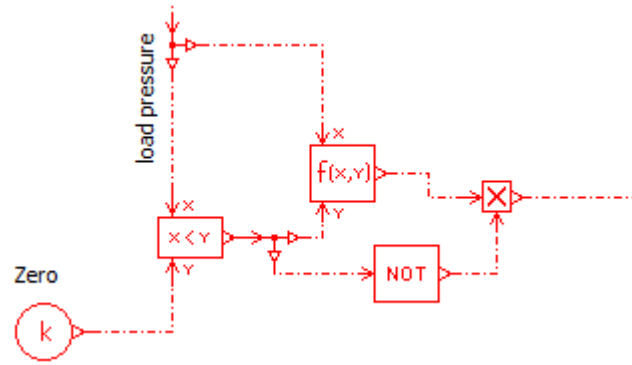


Figure 4-19: Logic conditions enforced to prevent the computation of the square root of a negative number at the starting instant of the simulation

On the contrary, in the first simulation instant, the load pressure results to be negative, hence, the condition expressed in the comparison block is met and its output is unitary. The formula block computes the expression $\sqrt{x+y}$, with y equal to 1 (corresponding to the “true” value exiting the comparison block). This result, even though non-null, is not anyway employed in the compensating flow computation since a logic “not”, whose output is multiplied by the formula block, inverts the result exiting the comparison block: therefore, the result of the computation, which is in this case useless, is prevented from propagating to the following components. No alterations would occur during proper operation, since the output of the logic “not” is unitary (because the output of the comparison block would be “false”, i.e. zero), therefore neutral in the multiplication.

Since no actual valve can be manufactured with a null overlap, a more realistic description of the control valve has been achieved by modifying the controller mathematical description by admitting an underlap U . Being x_v the valve spool displacement and U the negative overlap, the compensating flow rate Q_l is now generated as in **eq.4-10** and **eq.4-11**:

$$Q_l = \sqrt{p_s - p_l} \cdot x_v \cdot B \quad \text{if } x_v > U \quad \text{eq. 4-10}$$

$$Q_l = \sqrt{p_l - p_t} \cdot x_v \cdot B \quad \text{if } x_v < -U \quad \text{eq. 4-11}$$

During valve operation, when $|x_v| < U$, all passages results to be temporary connected and an additional flow Q_u is produced, defined as in **eq.4-12**:

$$Q_u = \sqrt{p_s - p_l} \cdot (x_v + U) \cdot B_1 + \sqrt{p_l - p_t} \cdot (x_v - U) \cdot B_2 \quad \text{eq. 4-12}$$

Even if negative overlap may lead to a certain loss in the liquid pressure, it prevents pressure peaks, hence shocks during start or stop and ensures a softer switching. **Figure 4-20** displays the modified controller logic, which takes into account the non-null overlap.

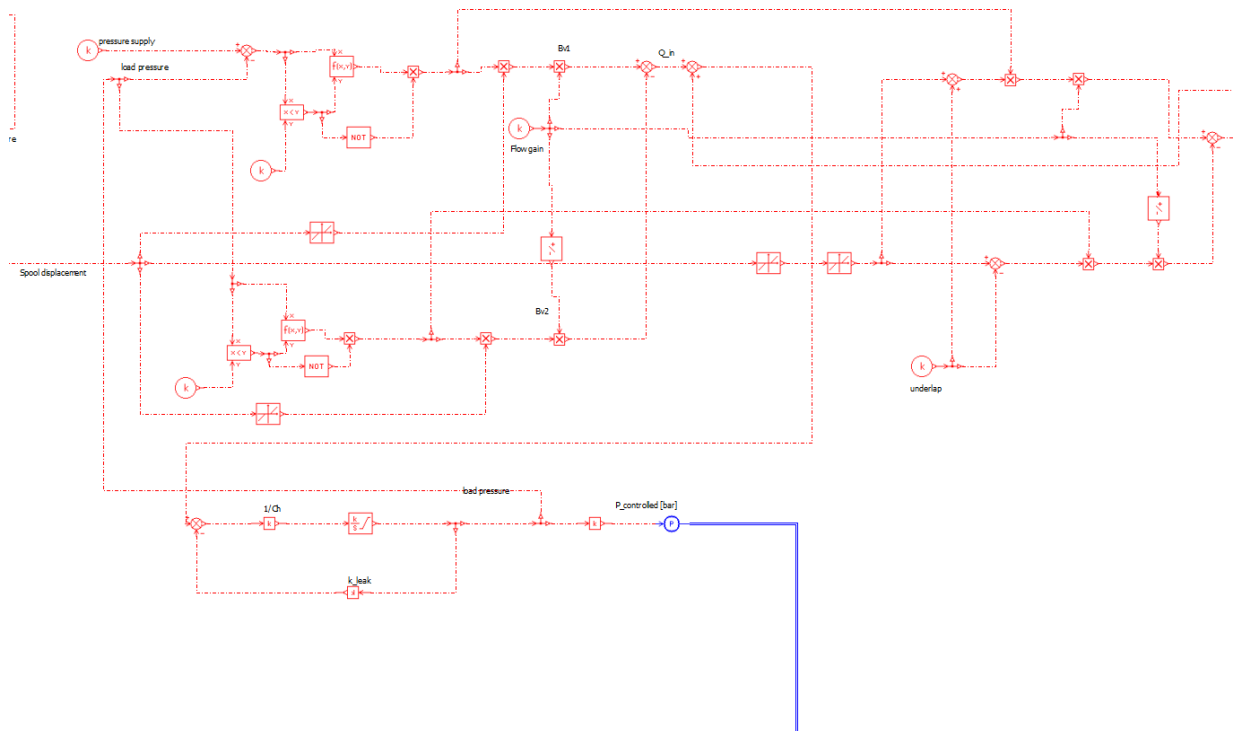


Figure 4-20: Modified simulation schematic which assumes an underlap in the control valve

Figure 4-21 illustrates the braking torque generated by the closed loop system when a harmonic disturbance has been injected to the system at the pads-rotor interface. The same set pressure has been considered (i.e. 50 bar) and the controller logic has been described by assuming null or negative overlap accordingly. As one can notice, the braking torque generated in the system featuring the control valve with underlap manifests a shorter and smoother transient.

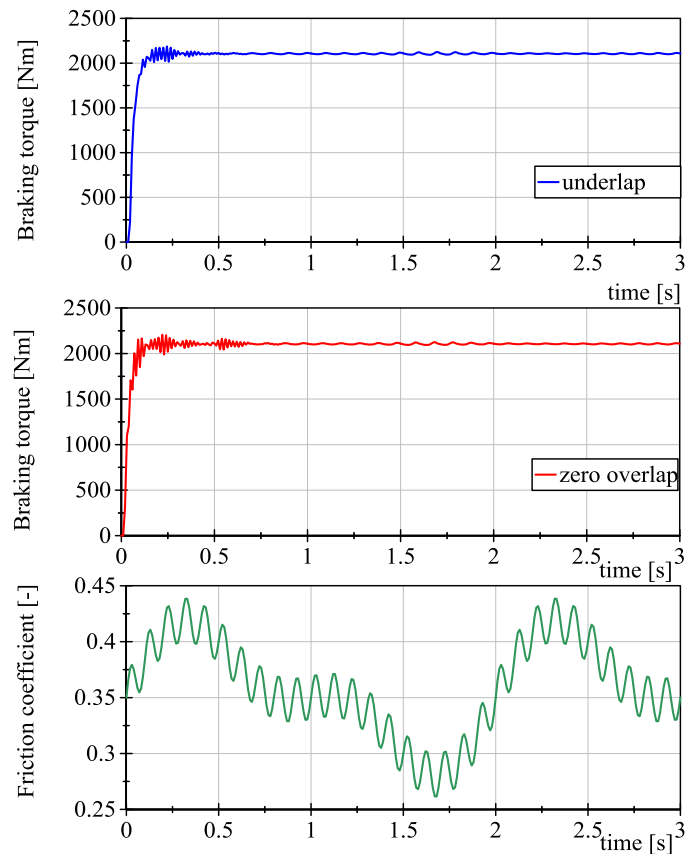


Figure 4-21: Response to a step input pressure signal in a closed loop system equipped respectively with a spool valve with negative overlap and null overlap, subjected to the same disturbance

4.2.3 Sensitivity analysis and parameters optimization

A sensitivity analysis has been undertaken using the Monte Carlo study tool offered by LMS Amesim, in order to investigate the influence of each parameter on the model overall behavior and to derive general guidelines to optimize the system performance.

The integral of the squared error (ISE) has been chosen as a performance indicator. Control systems specified to minimize ISE are usually suitable to perform a quick cancellation of large errors but are prone to tolerate small errors persisting for long time periods. This often leads to a fast response but with a lasting small-amplitude oscillation as a side effect.

For each of the variables relevant in the controller design a mean value was assumed and a suitable range of its standard deviation was set. A series of run were performed, with each of the parameters varying according a Gaussian distribution. In order to assess the individual influence of

each variable on the performance indicator, the batch tests were performed singularly, with a single parameter at a time considered variable and the others kept constant throughout the analysis.

As can be clearly seen from **Figure 4-22**, the ISE shows a decreasing trend with increasing values of the reciprocal of the valve mass. This can be justified since a smaller mass implies a reduced inertia, therefore a shorter response time.

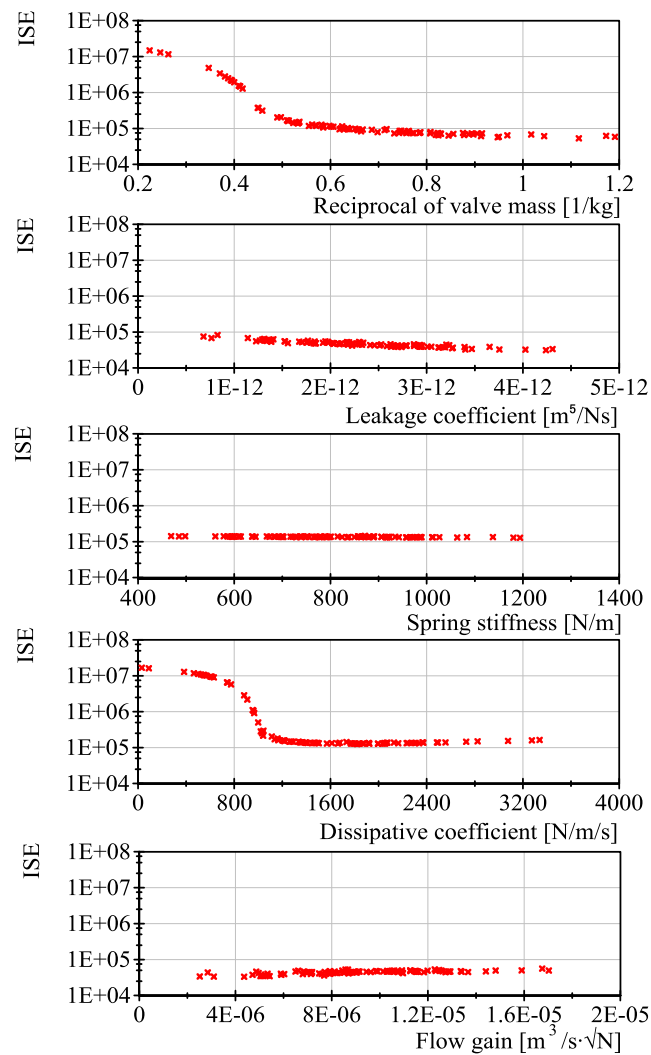


Figure 4-22: Scatter plots of ISE as function of different parameters

It is also apparent that high values of the dissipative coefficient are associated with a small value of the ISE. Nonetheless, these deductions have to be mediated with energy efficiency considerations, which would prevent to exaggerate the value of the above-mentioned parameter.

It can be noticed that variations of the spring stiffness, the leakage coefficient and the flow gain within the specified range don't lead to remarkable ISE excursions. Though, smaller values of the flow gain and relatively bigger ones of the leakage coefficient are still preferable. After carrying out the sensitivity analysis, the parameter set chosen has been further refined by running an optimization process, with the purpose of minimizing the ISE. LMS Amesim features two main tools to perform system optimization: NLPQL (nonlinear programming by quadratic Lagrangian) and the genetic algorithm. NLPQL is a sequential quadratic programming method for solving nonlinearly constrained optimization problems with differentiable objective and constrained functions. At each iteration, the search direction is given by the solution of a quadratic programming subproblem.

The genetic algorithm is a bio-inspired evolutionary metaheuristic algorithm. At each iteration step, a population of solution is generated and the best candidates are selected as "parents" to generate "children" for the following generation. Over successive the generations, the population evolves towards an optimal solution. Randomicity and diversity is added by means of mutations. Both the previously described methods are well-suited to nonlinear optimization problems; nevertheless, the genetic algorithm is usually less prone to get stuck into local minima and was therefore preferred. It also generally leads to longer runtime with respect to NLPQL, but since the optimization was performed "offline", this factor didn't represent an actual shortcoming. The parameters adopted for the optimization process are listed in **Table 4-2**.

Parameter	Value
Population size	100
Reproduction ratio	80%
Maximum number of generation	20
Mutation probability	10%
Mutation amplitude	0.2

Table 4-2: Genetic algorithm adopted parameters

4.2.4 Closed loop simulation results and stability analysis

Figure 4-23 shows the same load cycle which was proposed in **Figure 4-16**, performed with the novel active brake. The open loop behavior is represented in blue, while the closed loop curve is highlighted in red. It can be noticed that after a short transient with a modest overshoot, the set

point is achieved and the braking torque is held constant, despite the friction-coefficient variation. Thus, the closed-loop system fulfils the design goal.

Nonetheless, small ripples in the braking torque are still observable. This might be due to the choice of ISE as an objective function to optimize. A different purpose-oriented parametrization, as for instance the minimization of the IAE (Integral Absolute Error), would likely lead to a slower response with a less sustained oscillation.

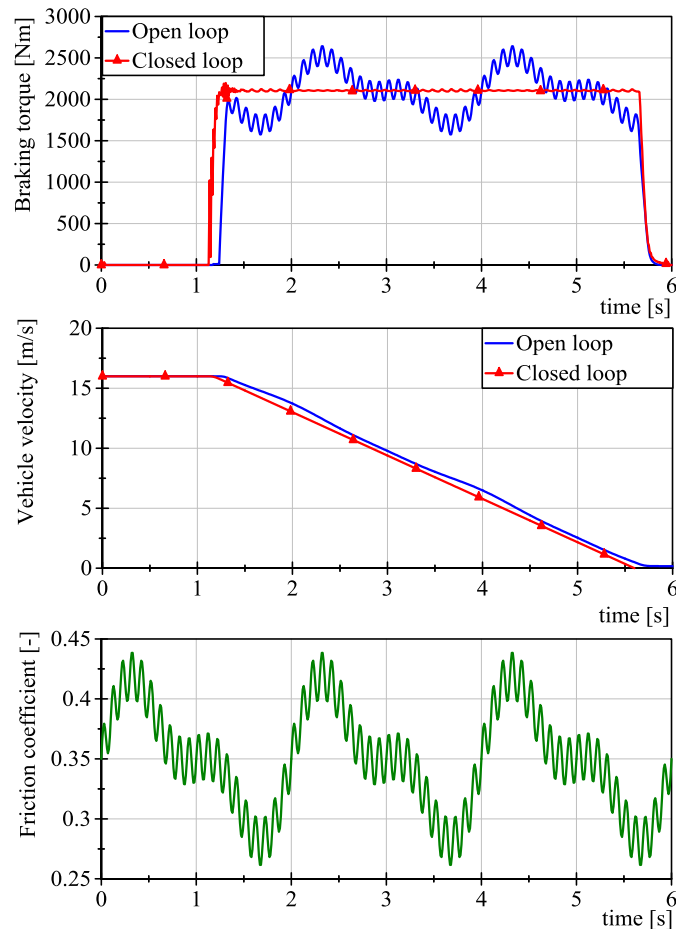


Figure 4-23: Simulated load cycle for the open loop and the closed loop system subjected to a pseudo-random pad-disc friction coefficient

In order to assess the closed loop system capabilities to prevent brake judder phenomena, the disturbance effect related to DTV was simulated too, as described in paragraph 4.1.2. The sine amplitude was set to 20 μm and a frequency of 10 Hz was considered. **Figure 4-24** illustrates its influence on the braking torque generated for a set pressure equal to 50 bar by the open and by the closed loop system, respectively.

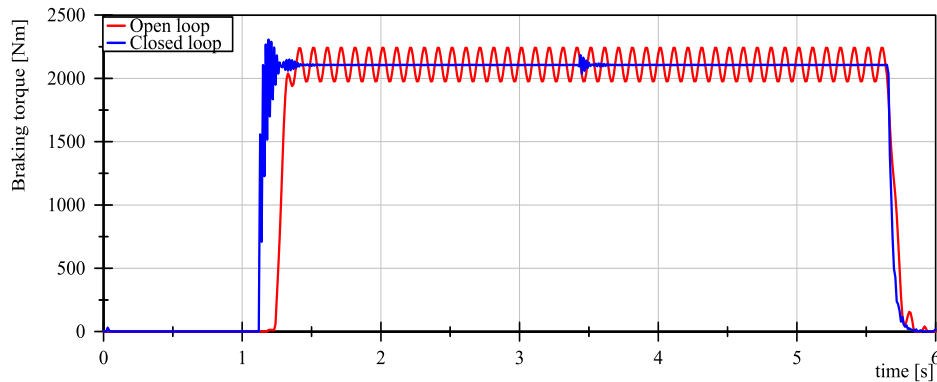


Figure 4-24: Generated braking torque by the open loop (red curve) and closed loop (blue curve) system when subjected to a DTV disturbance

If the closed loop system behaviour results to be satisfactory regardless of the injected disturbance for intermediate value of the set pressure, the same cannot be stated for the whole brake operating range. Indeed, as apparent from **Figure 4-25**, for low set pressure a remarkable overshoot is observable, while for high pressures (which approach the value of the constant pressure supply), the system is able to compensate only limited deviations from the braking torque theoretical value. This can be due to the value of the pressure drop across the control valve, namely $\Delta p = p_s - p_t$: if one recalls **eq.4-10**, the compensating volume flow rate Q_l results to be proportional to this pressure gradient, hence it is easy to envisage that high values of Δp would likely lead to overshoot, while small values of Δp might result in insufficient values of Q_l .

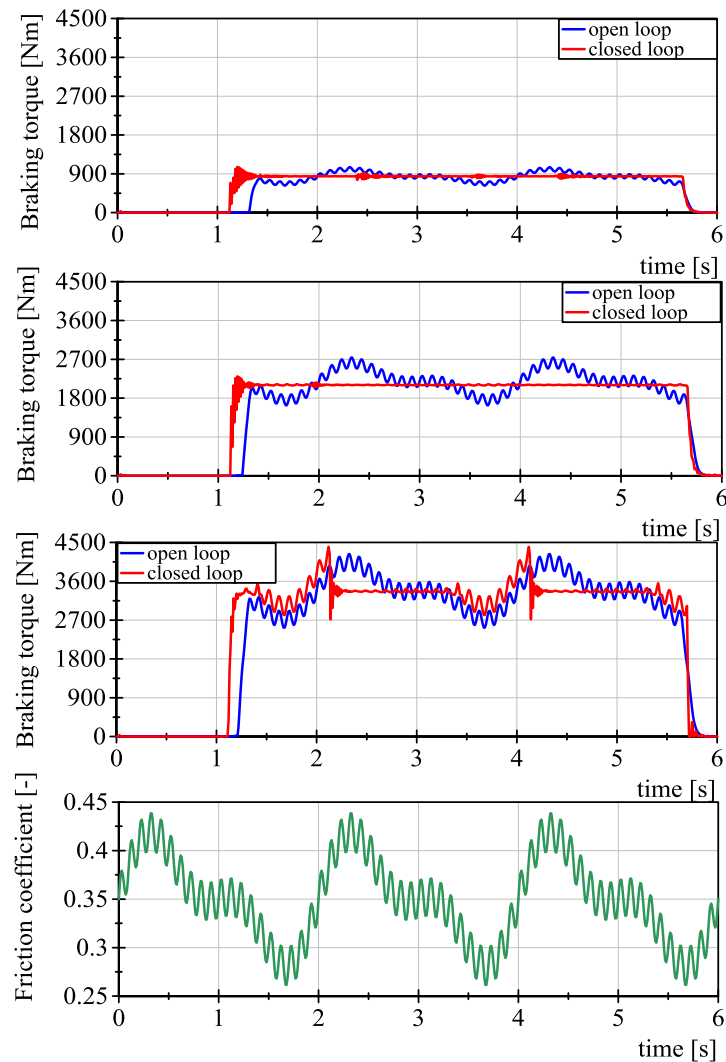


Figure 4-25: Generated braking torque by the open loop (red curve) and closed loop (blue curve) system when subjected to a pseudo-random pad-disc friction coefficient, for $p_{set}=20$ bar (top figure), $p_{set}=50$ bar (middle figure), $p_{set}=80$ bar (bottom figure).

An insight about the closed loop system dynamic performances within the brake operating range can be provided by **Figure 4-26**. The friction conditions variability at pads-rotor interface has been simulated by means of a sinusoidal signal with increasing frequency (0.1, 1, 10 Hz). While at low and intermediate set pressure the disturbance attenuation appears to be adequate, for high set pressure torque variations are partially compensated for medium frequency and hardly compensated at high frequency.

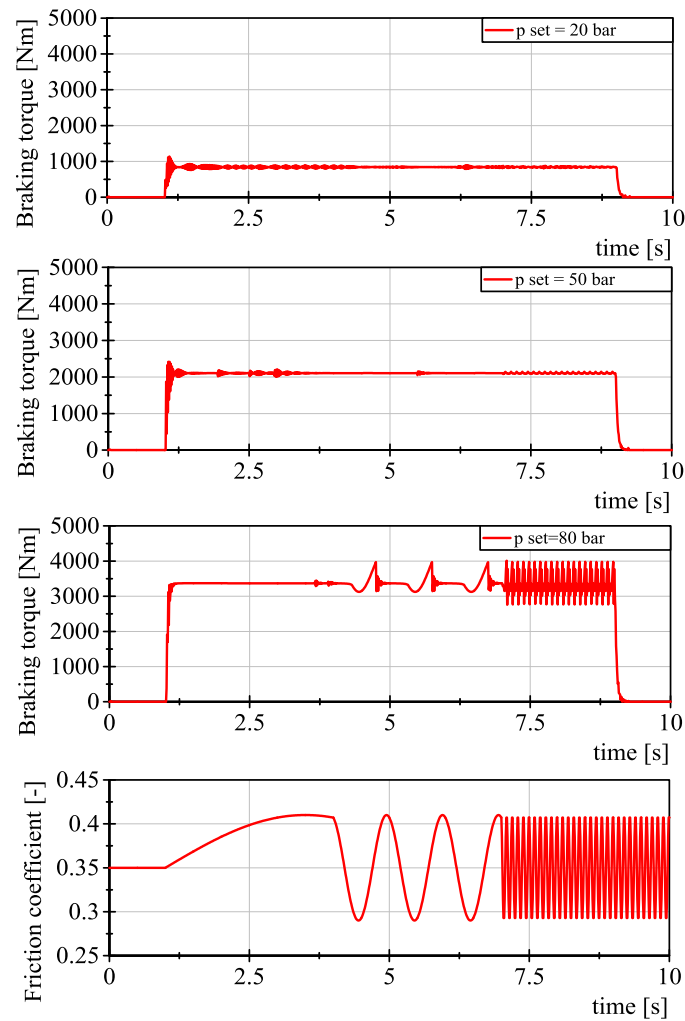


Figure 4-26: Braking torque generated for low, intermediate and high pressure regimes when a friction coefficient with sinusoidal trend and increasing frequency is applied

A more accurate analysis of the system dynamic response can be led by referring to the Bode plot shown in **Figure 4-27**, relative to the transfer function $T(s) = F_{s,actual} / F_{s,set}$. The system response has been investigated for low, intermediate and high set pressure (20, 50 and 80 bar respectively) considering the pressure operating range of the hydraulic actuator (0-92 bar).

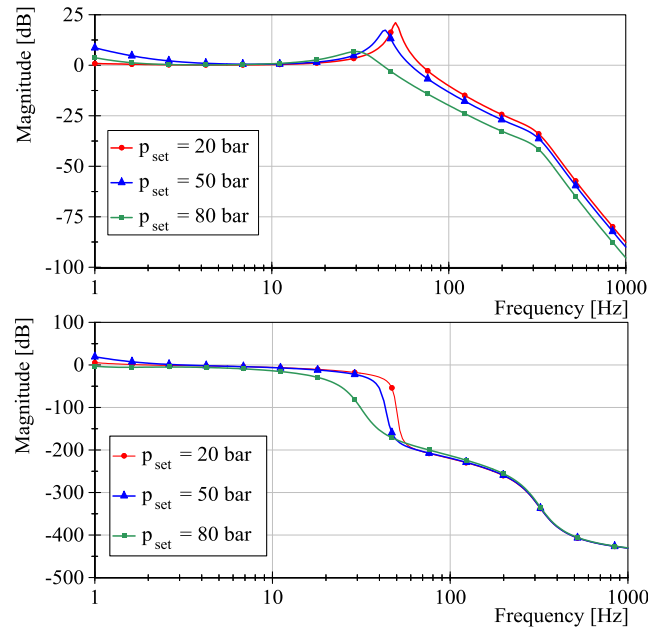


Figure 4-27: Magnitude and phase Bode plots relative to the transfer function $T(s)=F_{s,actual}/F_{s,set}$ obtained for a set pressure equal to 20,50,80 bar

As can be easily seen, the system dynamics decreases as the set pressure approaches the value of the pressure supply. With increasing set pressure, the resonance peak shifts to lower frequencies and becomes flatter. Namely, the resonance frequency varies from 30 to 50 Hz depending on the set pressure.

By recalling the controller block diagram structure represented in **Figure 3-19**, the closed loop stability can be evaluated by computing phase and gain margin from the Bode plot inherent to the open loop transfer function. In order to assess the closed loop stability according to this criterion, it is needed to verify the open loop stability first. This can be done by computing the poles of the open loop transfer function which with reference to the nomenclature adopted in the previous chapter, can be written as in **eq.4-13**:

$$T_o(s) = G_1(s) \cdot G_2(s) \cdot K \quad \text{eq. 4-13}$$

With the expressions for $G_1(s)$, $G_2(s)$ and K already presented in eq.3-87,3-88,3-89. Once it has been proved that all the poles of $T_o(s)$ lie within the left half of the s -plane, the Bode plot of the linearized open loop function can sensibly be exploited for closed loop stability considerations. As explained in paragraph 3.3.5, the system linearization has to be performed about a specific operating point: without loss of generality, the origin of the pressure-flow curves can be chosen as

suitable reference, being the most critical working condition from the stability viewpoint. Indeed, as can be observed from the equation of the flow gain k_{qx} and the pressure flow gain reported in **eq.4-14**, **4-15**, derived from /Mer67/, k_{qx} (which is directly related to the system gain) assumes its maximum value in the null operating point, while k_{px} (which can be referred to the system damping) has its minimum value in the origin of the pressure-flow curves.

$$k_{qx} = C_d \cdot w \cdot \sqrt{\frac{p_s - p_l}{\rho}} \quad \text{eq. 4-14}$$

$$k_{px} = \frac{C_d \cdot w \cdot x_v \cdot \sqrt{(1/\rho) \cdot (p_s - p_l)}}{2 \cdot (p_s - p_l)} \quad \text{eq. 4-15}$$

By computing k_{qx} and k_{px} for $p_r=Q_r=x_v=0$, one gets **eq.4-16**, **4-17**:

$$k_{qx} = C_d \cdot w \cdot \sqrt{\frac{p_s}{\rho}} \quad \text{eq. 4-16}$$

$$k_{px} = 0 \quad \text{eq. 4-17}$$

The magnitude and phase Bode plots relative to $T_o(s)$ are displayed in **Figure 4-28**. The phase and gain margin inherent to the null operating condition are highlighted in **Table 4-3**.

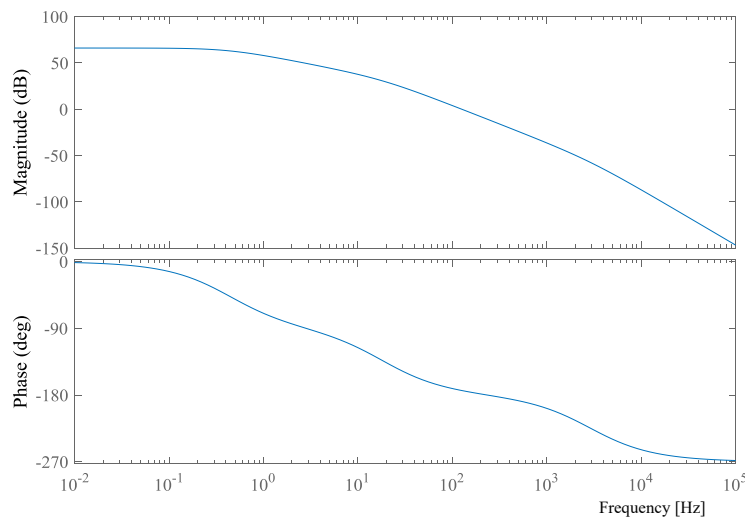


Figure 4-28: Magnitude and phase Bode plots relative to the open loop transfer function $T_o(s)$.

Gain Margin [dB]	Phase Margin [°]	Stability
10.7	6.03	✓

Table 4-3: Gain and phase margins computation in the null operating point

As can be inferred from the table shown above, the closed loop system is stable even in its most critical working point. However, the phase margin appears to be particularly narrow (ideally, a value around 30° would be desirable); a more robust design could be accomplished by adopting a variable pressure source in order to limit the difference between supply pressure and load pressure within the whole system operating range, reducing k_{qx} (hence, the open loop gain) and increasing k_{px} (thus, the system damping). In support of this argument, the phase and gain margins for a low, intermediate and high set pressure (i.e. 20, 50 and 80 bar respectively, bearing in mind the supply pressure p_s is equal to 92 bar) have been reported in **Table 4-4**.

P_{set} [bar]	Gain Margin [dB]	Phase Margin [°]	Stability
20	13	8.17	✓
50	17.1	12.7	✓
80	26.3	28.8	✓

Table 4-4: Gain and phase margins computation for the set pressure of 20, 50, 80 bar

To provide a more thorough analysis of the influence of the Δp , the pressure drop across the valve, on the closed loop system dynamic behaviour, the Bode plots in **Figure 4-28** have been obtained for a constant set pressure ($p_{set}=50$ bar) and variable value of the pressure supply (i.e., 65,80 and 95 bar).

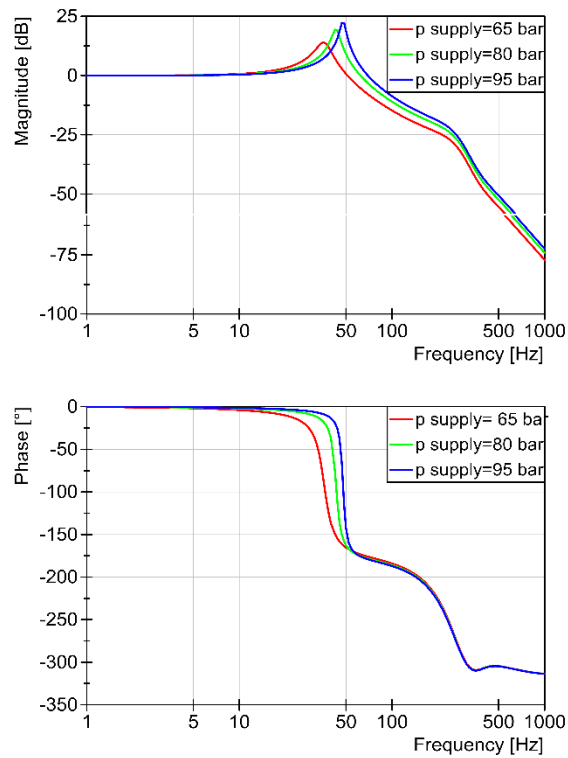


Figure 4-29: Magnitude and phase Bode plots relative to the transfer function $T(s)=F_{s,actual}/F_{s,set}$ obtained for a set pressure equal 50 bar for variable values of the pressure supply

As it is apparent from the diagrams above, as Δp becomes bigger, the resonance peak gets higher and it is shifted to higher frequencies; meanwhile, gain and phase margins narrow progressively.

5 Summary and outlook

In the present work, an active disc brake system for light railway applications has been thoroughly analysed by using the software LMS Amesim.

The main criticalities and disturbance sources affecting the system proper operation have been detected and highlighted, with particular reference to the complex tribological phenomena at pads-rotor interface, related to the occurrence of brake judder and brake fade. In order to ensure the safety and repeatability of the braking performance regardless of the system operating conditions, a closed loop approach has been proposed, envisaging the embedding of a hydro-mechanical control unit in the standardized brake design.

The force measured along the supporting pole of the brake assembly has been proven to be suitable to assess system proper operation, since it is proportional to the actual braking torque. Thus, it has been exploited as feedback signal, to be conveyed on one end of a control spool valve, which would receive a reference signal on the opposite end.

The valve spool moves in order to establish force balance, hence matching between the set torque and the actual one. Connecting alternatively the valve outlet to the pressure supply or to the tank, the valve produces a pressure rise in the hydraulic actuator when the set force exceeds the feedback one, while it generates a pressure drop when the force acting along the support pole results to be bigger than the reference signal.

After a parametrization, the control concept has been embedded into the brake simulation model and the performances of the original and of the novel system in perturbed conditions have been compared. A sensitivity analysis has been conducted to deduce general guidelines for the system design, while the optimization performed by means of the genetic algorithm has allowed to refine the initial parameters set.

Although the adoption of the closed loop concept is undoubtedly beneficial since the enhanced system always shows an improved behavior with respect to the original one, performances are not equally satisfactory within the whole brake operating range.

While at intermediate set pressure the system behaves ideally, for low pressure it displays a remarkable overshoot in its step response and it is prone to instability. At high set pressures instead, it can compensate just partially the deviations of the braking torque from its set value. A sensitive solution would lie in the assumption of a tunable pressure supply, which would ensure an adequate pressure drop across the control valve. Hence, a suitable trade-off between the system robustness and its capability to generate a sufficient compensating volume flow rate.

Future work will involve the validation of this assumption, the design of a prototype, its manufacturing and a measurement on a test rig.

III Literature

- /ACO16/ ACO-Eurobar „Continuous cast iron: Ductile iron EN-GJS-400-18C-LT”, ACO-Eurobar datasheet, May 2016
- /And90/ Anderson A.E. „Friction, Lubrication and Wear Technology”, ASM Hand Book, ASM Materials Information Society, USA, 1990
- /Bea99/ Beater P. „Entwurf hydraulischer Maschinen: Modellbildung, Stabilitätsanalyse und Simulation hydrostatischer Antriebe und Steuerungen”, Springer, 1999
- /Bha06/ Bhabani K., Sata- pathy K., Bijwe J. „Composite friction materials based on organic fibres: Sensitivity of friction and wear to operating variables”, Composites: Part A 37, 2006
- /BOS16/ Bundesrepublik Deutschland „Straßenbahn-Bau und Betriebsordnung“, December 2016
- /Bre12/ Breuer B., Bill K.H. „Bremshandbuch“, Springer, 2012
- /Cru12/ Cruceanu C. „Train braking, reliability and safety in railway”, Dr. Xavier Perpinya (Ed.), InTech, 2012
- /Cun02/ Cundiff J. S. „Fluid power circuits and controls: fundamentals and applications”, CRC Press, 2002
- /Dra10/ Drabison J.S. „Experimental Investigation of Judder in a Floating Disc-Caliper Braking System with Focus on Pad Geometry”, Master Thesis, Ohio State University, 2010
- /Dry56/ Dryden H. L., Murnaghan D.F., Bateman H. „Hydrodynamics”, Dover Publishing, New York, 1956
- /Gen12/ Gent A.N. „Engineering with rubber”, Hansen, 2012
- /Gil05/ Gilles T. „Automotive Chassis: Brakes, Suspensions and Steering“, Delmar Learning, 2005
- /Han16/ Hanning&Kahl „Brake with a system“, available online: <https://www.hanning-kahl.de/produkte/hydraulische-bremssysteme/systembeschreibungen.html>
- /Lee13/ Lee C., Manzie C. „Adaptive Braking torque Variation Compensation for an Electromechanical Brake“, SAE Int. J. Passeng. Cars - Electron. Electr. Syst. / Volume 5, Issue 2, 2013
- /Lee15/ Lee N.J., Kang C.G. „The effect of a variable disc pad friction coefficient for the mechanical brake system of a railway vehicle“, PLoS ONE 10(8):e0135459, 2015
- /LMS16/ LMS Imagine.Lab Amesim „HYD Advanced Fluid Properties“, Technical Bulletin n.117, LMS Imagine.Lab Amesim User’s Guides, Siemens Industry Software NV, 2016

- /Lun15/ Lundin Christopher „Modelling of a hydraulic braking system”, KTH electrical engineering master thesis, Stockholm 2015
- /Mag14/ Magnier V., Brunel J.F., Dufrénoy P. „Impact of contact stiffness heterogeneities on friction-induced vibration“, International Journal of Solids and Structures, 2014
- /Mar14/ Martinez C.M. et al. „Modelling and estimation of friction braking torque for a brake by wire system”, IEEE IEVC, Florence, 2014
- /Mat18/ MathWorks „Modelling directional valves”, Simscape fluids documentation, R2018a
- /Mer67/ Merritt H. „Hydraulic Control Systems”, Wiley, 1967
- /Mit17/ Mitsumoto M. „Copper free brake pad with stable friction coefficient”, Hitachi Technical Report no.59, March 2017
- /Moh03/ Mohieddine J., Kroll A. „Hydraulic Servo Systems: Modelling, Identification and Control”, Springer, 2003
- /Oga70/ Ogata, Katsuhiko „Modern control engineering”, Englewood Cliffs, Prentice Hall, 1970
- /Ose17/ Osenin Y. et al. „Providing stable friction properties of disc brakes for railway vehicles“, Transport Problem, 2017
- /Pan97/ Panagin R. „La dinamica del veicolo ferroviario“, Editrice Universitaria Levrotto & Bella, Torino, 1997
- /Pen06/ Deutsche Pentosin Werke GmbH Pentopol J32 Product Datasheet, 2006
- /Pet16/ Petry M., Murrenhoff H. „Reduktion von Bremskraftschwankungen mithilfe einer Selbstverstärkenden Elektro-Hydraulischen Bremse“, Fluidtechnik O+P, 7-8/2016
- /Pet17/ Petry M., Zaki A., Murrenhoff H. „Disc brake with hydromechanically controlled braking torque for railway applications“, the 10th JFPS International Symposium on Fluid Power, Fukuoka, 2017
- /Rei14/ Reif K. „Brakes, brake control and driver assistance systems: function, regulation and components“, Bosch professional automotive information, Springer Vieweg, 2014
- /Sha15/ Sharma R. C., Dhingra M., Pathak R.K. „Braking systems in railway vehicles“, International Journal of Engineering, Research & Technology, Vol.4 Issue 01, January 2015
- /UIC13/ International Union of Railways UIC leaflet 544-1, „Brakes-braking performance“, 5th edn., June 2013
- /Wat99/ Watany S. et al. „Brake squeal generation”, SAE Technical Paper, 1999
- /Yun10/ Yun S.M. et al. „Proportional pressure reducing valve for clutch control

-
- system“, International Conference on Control, Automation and Systems, Korea, 2010
- /Zak16/ Zaki Ahmed „Entwicklung einer hydraulisch-mechanischen Schiebenbremse“, IFAS Bachelorarbeit, Aachen, 2016
- /Zha10/ Zhang L.J., Pang M. „Effect of disc thickness variation on antilock braking system“, Proceedings of ISMA , 2010

IV List of figures

Figure 2-1:	Blending and braking force partitioning as a function of the vehicle velocity /Bre12/	12
Figure 2-2:	Indirect pneumatic brakes working principle schematic /Bre12/. 1. Pressure supply 2. Air reservoir 3. Brake signal valve 4. Control valve 5. Air supply reservoir 6. Brake cylinder	13
Figure 2-3:	Overview of the braking equipment featured by the light rail vehicle Flexity Classic /Han16/	19
Figure 2-4:	A passive fail-safe brake in the released position (on the left) and in the applied position (on the right) /Zak16/	19
Figure 2-5:	Active brake in the released position (on the left) and in the applied position (on the right) /Zak16/	20
Figure 3-1:	Active brake caliper HYA 48/72 by Hanning & Kahl /Han16/	25
Figure 3-2:	Floating caliper fundamental components /Gil05/	26
Figure 3-3:	Clamping force/input pressure characteristic of the hydraulic actuator (Courtesy of Hanning&Kahl)	27
Figure 3-4:	Hydraulic circuit of the hydraulic power unit HZY-K140-APR (Courtesy of Hanning & Kahl).	29
Figure 3-5:	Schematic of the simplified braking system	30
Figure 3-6:	Schematic of a direct operated pressure reducing valve /Yun10/	31
Figure 3-7:	RC schematic of the hydraulic line	33
Figure 3-8:	Dynamic response of pressure p_2 to a step input change	34
Figure 3-9:	Hydraulic actuator simplified representation	34
Figure 3-10:	Brake assembly schematic	36
Figure 3-11:	Closed loop concept schematic	38
Figure 3-12:	4/2-way spool valve /Mat18/	40
Figure 3-13:	Electric equivalent circuit of a 4/2 spool valve /Lun15/	40
Figure 3-14:	Leakage flowrate trend with respect to spool displacement /Moh03/	42
Figure 3-15:	Closed loop system block diagram	46
Figure 3-16:	Closed loop system block diagram	46
Figure 4-1:	Overview of the LMS Amesim simulation model of the open loop braking system	51
Figure 4-2:	Hydraulic components of the simulation model: PPRV, pipeline connection, hydraulic actuator	52

Figure 4-3:	Simplified model of the PPRV	53
Figure 4-4:	Input pressure to the hydraulic actuator (in blue) compared to pressure signal output from PPRV (in red)	53
Figure 4-5:	Hysteresis cycle for the passive brake HYS258re (courtesy of Hanning&Kahl)	55
Figure 4-6:	Input pressure/Clamping force characteristic of the hydraulic actuator	56
Figure 4-7:	Elastic contact modules on rotor inboard and outboard sides	56
Figure 4-8:	Effect of DTV disturbance on the generated braking torque of a system equipped with “soft” pads (in red) and of a system featuring stiff pads (in blue)	57
Figure 4-9:	Effect of temperature variation on clamping force due to the change of fluid viscosity	58
Figure 4-10:	Friction coefficient as a function of temperature, deceleration and vehicle velocity variation	60
Figure 4-11:	Active brake kinematic model	61
Figure 4-12:	Amesim 3D kinematic model	61
Figure 4-13:	Computation of the effective braking radius	62
Figure 4-14:	F_s and T_{br} relationship for different input pressure and in ideal and perturbed conditions	63
Figure 4-15:	α dependency on variable rotor displacements along x and z direction	64
Figure 4-16:	Exemplary load cycles simulated for a constant (red curve) and a pseudo-random (blue curve) friction coefficient at disc-pad interface	65
Figure 4-17:	Simulink controller logic	68
Figure 4-18:	Controller logic embedded in Amesim simulation model	69
Figure 4-19:	Logic conditions enforced to prevent the computation of the square root of a negative number at the starting instant of the simulation	70
Figure 4-20:	Modified simulation schematic which assumes an underlap in the control valve	71
Figure 4-21:	Response to a step input pressure signal in a closed loop system equipped respectively with a spool valve with negative overlap and null overlap, subjected to the same disturbance	72
Figure 4-22:	Scatter plots of ISE as function of different parameters	73
Figure 4-23:	Simulated load cycle for the open loop and the closed loop system subjected to a pseudo-random pad-disc friction coefficient	75
Figure 4-24:	Generated braking torque by the open loop (red curve) and closed loop (blue curve) system when subjected to a DTV disturbance	76

Figure 4-25: Generated braking torque by the open loop (red curve) and closed loop (blue curve) system when subjected to a pseudo-random pad-disc friction coefficient, for $p_{set}= 20$ bar (top figure), $p_{set}= 50$ bar (middle figure), $p_{set}= 80$ bar (bottom figure).77

Figure 4-26: Braking torque generated for low, intermediate and high pressure regimes when a friction coefficient with sinusoidal trend and increasing frequency is applied 78

Figure 4-27: Magnitude and phase Bode plots relative to the transfer function $T(s)=F_{s,actual}/F_{s,set}$ obtained for a set pressure equal to 20,50,80 bar 79

Figure 4-28: Magnitude and phase Bode plots relative to the open loop transfer function $T_o(s)$ 80

Figure 4-29: Magnitude and phase Bode plots relative to the transfer function $T(s)=F_{s,actual}/F_{s,set}$ obtained for a set pressure equal 50 bar for variable values of the pressure supply82

V List of tables

Table 2-1: Time limit for brake application and brake release for rail vehicles of type “G” and “P”	13
Table 2-2: Main braking regimes classification	14
Table 2-3: Minimum deceleration requirements prescribed by BOStrab for light rail vehicle ..	18
Table 3-1: Mechanical and physical properties and admissible operating range of Jurid 809 (Courtesy of Honeywell)	28
Table 3-2: Fluid properties of Pentopol J32 (Courtesy of Pentosin).....	29
Table 4-1: Simulation parameters assumed for the hydraulic actuator model	54
Table 4-2: Genetic algorithm adopted parameters	74
Table 4-3: Gain and phase margins computation in the null operating point	81
Table 4-4: Gain and phase margins computation for the set pressure of 20, 50, 80 bar	81

